JOHANNES GUTENBERG-UNIVERSITÄT MAINZ

Phase transitions of aqueous solutions under pressure

by

Sadeed Hameed

August 2023

Bachelor Thesis in Physics
Submitted to the Faculty of Physics of the
Johannes Gutenberg-Universität Mainz

1st Supervisor: Prof. Dr. Katrin Amann-Winkel
2nd Supervisor: Prof. Dr. Thomas Palberg

Ich versichere, dass ich die Arbeit selbstständig verfasst und keine anderen als die angegebenen Quellen und Hilfsmittel benutzt sowie Zitate kenntlich gemacht habe.

Mainz, den 31. August 2023

Sadeed Hameed

Johannes Gutenberg-Universität D-55099 Mainz

shameed@students.uni-mainz.de

Contents

1   Introduction

> 'Flüssigkeit ist was fürchterlich Kompliziertes. Und wir wissen nun auch gar
> nicht, was eigentlich das Wasser ist, diese "einfache" Substanz.'[1]
>
> Friedrich Hund, 1979

Water exhibits numerous anomalous properties compared to other liquids and solids. One well-known fact is its density maximum at about $4\,°C$ at ambient pressure and there are many more of these atypical properties (e.g. its comparably high melting and boiling point or the large variety of (meta-)stable crystalline and amorphous phases).[2]

It is also the first one-component substance for which more than one amorphous structure, namely low-density amorphous ice (LDA) and high-density amorphous ice (HDA), was observed, a property which is now referred to as "polyamorphism".[3]

Computer simulations and experimental studies suggest a scenario where the transition between LDA and HDA continues as a liquid-liquid transition (LLT) for higher temperatures and ends in a possible second critical point, the so-called liquid-liquid critical point (LLCP).[4]

While the exact position and even the existence of it are still debated, the LLCP is expected to be located above the crystallization and below the homogenous nucleation temperature, a region of the phase diagram called "no man's land", making water under ambient conditions a supercritical state of those two liquids, possibly explaining the anomalies as results of fluctuations between these two liquids.[4]

However, rapid crystallization in the "no man's land" prevents one to experimentally study supercooled water in this region of the phase diagram.

One possibility to access the no man's land experimentally, could be the use of aqueous solutions which hinder crystallization, but still behave water-like to a certain degree of dilution.

In this thesis, amorphous phase transitions of pure water and polar aqueous solutions (glycerol, sorbitol and erythritol) are studied by using a piston-cylinder setup, which allows measurement of density changes by varying pressure and temperature. Furthermore, X-ray powder diffraction will be used to characterize the prepared samples.

2   Supercooled water and aqueous solutions

One of the unique properties of water is its large variety of crystalline phases. Today, 20 different forms of crystalline ice are known.[5]

While hexagonal ice (I_h), cubic ice (I_c) and ice VI can be found on the earth, the other crystalline phases of ice are more abundant in outer space.[5]

But one can supercool water if nucleation is prevented. For pure water, this is possible to temperatures above the so-called homogenous nucleation temperature T_H, where nucleation in the pure sample will lead to rapid crystallization.

Below this homogenous nucleation temperature T_H and above the crystallization temperature T_X, rapid crystallization makes it difficult to study amorphous water experimentally. There are multiple ways to make amorphous water:

- Pressure-induced amorphization (PIA) is a technique implemented by Mishima to make unannealed high-density amorphous ice (uHDA) by compressing ice I_h at about $77\,\text{K}$ to pressures above $1\,\text{GPa}$.[6]

- Vapour deposition of water molecules onto a smooth, cold ($< -110\,^\circ\text{C}$) substrate leads to a diffuse halo in the observed X-ray pattern, indicating its amorphous structure and was first observed in 1935.[7] The amorphous ice made by using this technique is also called amorphous solid water (ASW).

- Vitrification of μm-sized aerosols of water or aqueous solutions was first implemented by Brüggeller and Mayer in 1980 by plunging them into liquid ethane or propane as cryomedium.[8] Due to its importance for studying biological samples using cryogenic electron microscopy, Jacques Dubochet received the Nobel Prize in chemistry in 2017 for his contributions in using a thin layer of such vitrified water to hinder aggregation.[9] In 1985, Mayer developed the so-called hyperquenching technique, in which high cooling rates (10^6 to $10^7\,\text{K/s}$) can be achieved by depositing the aerosols on to a cryoplate in vacuum using a supersonic flow.[10] Amorphous water made this way is called hyperquenched glassy water (HGW).

For this thesis, the amorphous samples will be made using the PIA technique (see Section 3.1). In Table 1 the preparation methods, as well as the densities of the different amorphous ices are summarized.

The phase diagram of non-crystalline water is shown in Figure 1.

	Acronym	Preparation	Density [g/m^3]
LDA	ASW	Vapour deposition[7,11]	0.94[12]
	HGW	Hyperquenching[13]	0.94[12]
	LDA-I	Heating uHDA at < 0.1 GPa to 130 K[14,15]	0.94[12]
	LDA-II	Decompression of VHDA at 140 K to ≤ 0.05 GPa[15–17]	0.94[15]
HDA	uHDA	Compression of ice I$_h$ at 77 K to > 1.2 GPa[6]	1.15[18]
	eHDA	Annealing uHDA at $0.18 - 0.30$ GPa to 130 K[19]	-
		Decompression of VHDA at 140 K to 0.07 GPa[16,17]	1.13[21]
		Compression of LDA at $130 - 140$ K to > 0.4 GPa[20]	-
VHDA	VHDA	Annealing uHDA at ≥ 0.8 GPa to > 160 K[18]	1.26[18]
		Compression of LDA at ≥ 125 K to ≥ 1.2 GPa[22]	-
		Compression of ice I$_h$ at ≥ 130 K to ≥ 1.2 GPa[23]	-

Table 1: Preparation and densities of the different amorphous ices. (Table adapted from reference [21])
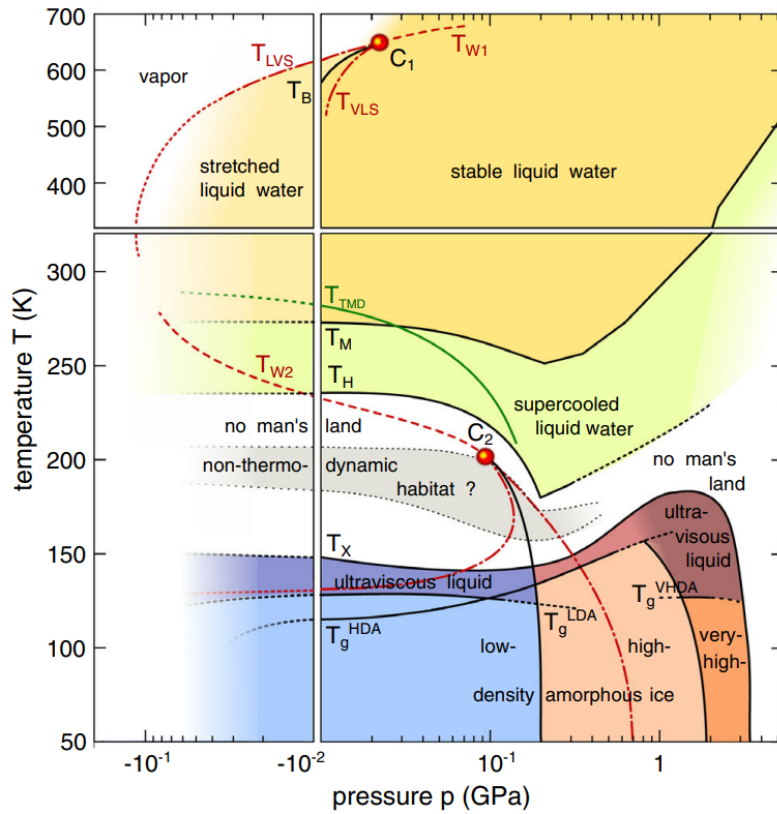
Figure 1: Phase diagram of non-crystalline water. (Diagram taken from [24])

Mishima et al. showed that there is a reversible first-order transition between LDA and HDA.[14] Computational studies show that this transition continues as a liquid-liquid transition (LLT) between low-density liquid (LDL) and high-density liquid (HDL) for higher temperatures and could end in a second critical point, the liquid-liquid critical point (LLCP)[4], which was first suggested by Poole et al. using molecular dynamics simulation (ST2 model) in 1992.[25]

However, the LLCP (marked as C_2 in Figure 1) is expected to be located in the no man's land, where amorphous water is hard to investigate experimentally due to the rapid crystallization mentioned before.

There are efforts to bypass the limit for experimental studies in the no man's land. One possibility to do so could be the study of dilute aqueous solutions, e.g. polar and ionic solutes, which hinder crystallization by interacting with the solvent water. Computer simulations as well as experimental studies show that the solutions have LDA- and HDA-like phase behaviour.[26] Also, the transition between those two could be observed for temperatures above the glass transition temperatures of LDA and HDA, indicating the existence of the LLT.[27]

As shown for glycerol solutions in Figure 2, the phase diagram of binary aqueous solutions depends not only on pressure and temperature but also on the concentration of the solute, stated in mole fraction (mf), possibly shifting the LLT and LLCP to a more accessible region.[26] The aim of such studies with aqueous solutions is to investigate the amorphous phase behaviour of the solutions for varying concentrations in order to extrapolate the inaccessible region of the phase diagram of pure water from it.
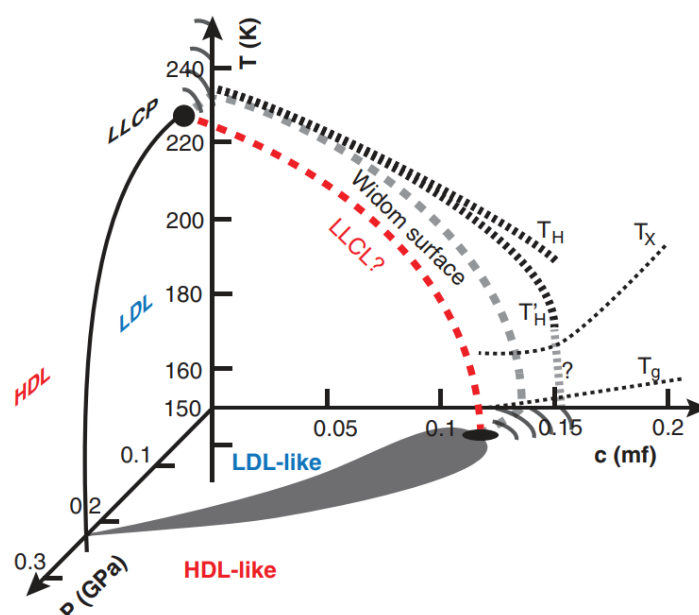
Figure 2: Schematic phase diagram of glycerol-water solutions. (Diagram adapted from [27])

Previous studies on amorphous transitions of dilute glycerol solutions mainly focused on samples made by pressure-vitrification (PVI).[27–29] The solutions are vitrified by cooling them at a high enough rate ($\sim 40\,\mathrm{K/min}$) at a pressure of $\sim 0.3\,\mathrm{GPa}$ leading to a homogeneous high-density glassy sample.[28]

Experimental studies regarding the polyamorphic transition in samples of aqueous solutions made by PIA, where the samples are first quenched to $77\,\mathrm{K}$ at ambient pressure and then compressed, are still rare. It was suggested that in contrast to homogenously dispersed samples made by PVI, samples of glycerol-water solutions made by PIA are heterogenous due to segregation of ice crystals during cooling at ambient pressure, leaving behind a maximally freeze-concentrated solution (MFCS), as sketched in the second column of Figure 3.[30] There are glassy MFCS domains with a concentration of $0.38\,\mathrm{mf}$ (green) which in contrast to the surrounding ice domains (white) cannot undergo PIA. Between those two domains, there is a so-called "interphase" (gray) consisting of "distorted ice" which is expected to also not undergo PIA.
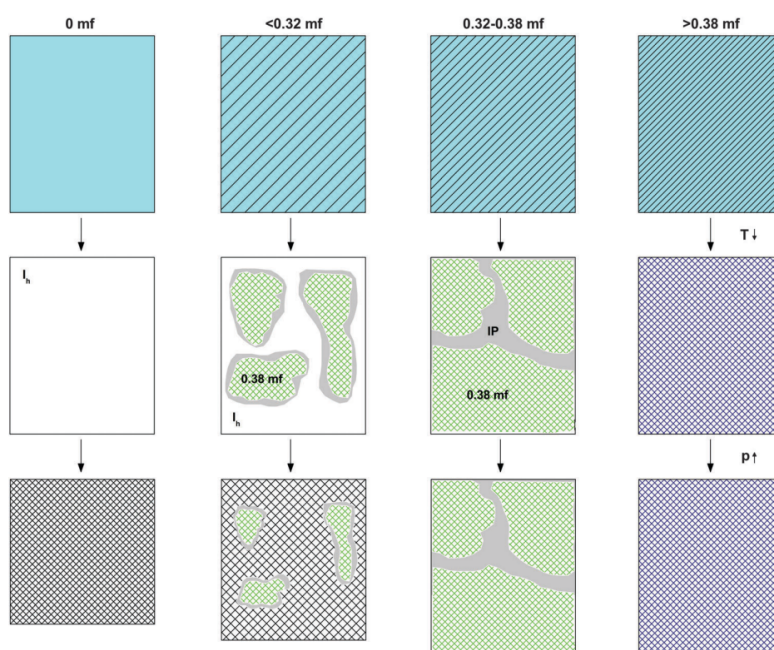
Figure 3: Sketch indicating phase separation upon cooling dilute glycerol solutions under ambient conditions to $77\,\mathrm{K}$. (Picture taken from [30])

Besides glycerol, this thesis also examines samples of sorbitol and erythritol solutions produced by PIA, which allows a comparison with PVI measurements for these substances conducted by Suzuki.[28] This may also allow identifying differences between the high-density solutions made via PVI and PIA, as this is still an open question for experimental studies with aqueous solutions, since only measurements of LiCl and glycerol have been done using both techniques.[26]

3 Experimental methods

3.1 Piston-cylinder apparatus

Figure 4: ZwickRoell Z100 TL testing machine

Using the ZwickRoell Z100 TL testing machine (Figure 4) a piston-cylinder setup according to Figure 5a is implemented, allowing one to conduct high-pressure ice experiments, as well as generating various samples of high-pressure ice phases. With a maximum applicable force of 100 kN, it is possible to investigate samples at pressures up to 2 GPa. For this, a cylindrical steel cell (Figure 5b) is used which contains a vertical drill-hole with a diameter of $8\,$mm in its centre. In this drill-hole steel pistons of different sizes are inserted, between which one places an indium container containing the $400\,\mu$l sample (one measurement (SH21) was done with a $500\,\mu$l sample). For pure water, the sample volume is determined with a pipette to an accuracy of $1\,\mu$l, whereas for the aqueous solutions it is measured to an accuracy of $10\,\mu$l using a syringe. The indium containers are made from a $0.2 \times 25 \times 25\,$mm indium foil. Indium is used in order to decrease friction within the cell, which could lead to unwanted heat evolution and thus possible crystallization.

Three additional drill holes of $4\,$mm diameter are used for temperature control with an Eurotherm 3508 temperature controller.

Furthermore, the cell is placed within a coil through which liquid nitrogen can circulate using a vacuum pump (Leybold SOGEVAC SV 25 D) and a pot in which liquid nitrogen will be filled, thus cooling the sample to approximately $77\,$K.

Additional steel plates and discs are used for an even pressure distribution, while teflon

and bakelite are specifically used as materials due to their low thermal conductivity. The exact specifications for the components of the piston-cylinder setup can be found in the appendix (Table 5).

The different compression and decompression runs can be automated using the testXpertIII software.

The combined measurement of applied pressure, temperature and piston displacement makes it possible to characterize phase transitions of ice samples.

(a) CAD of the whole setup   **(b)** Sketch of steel cell
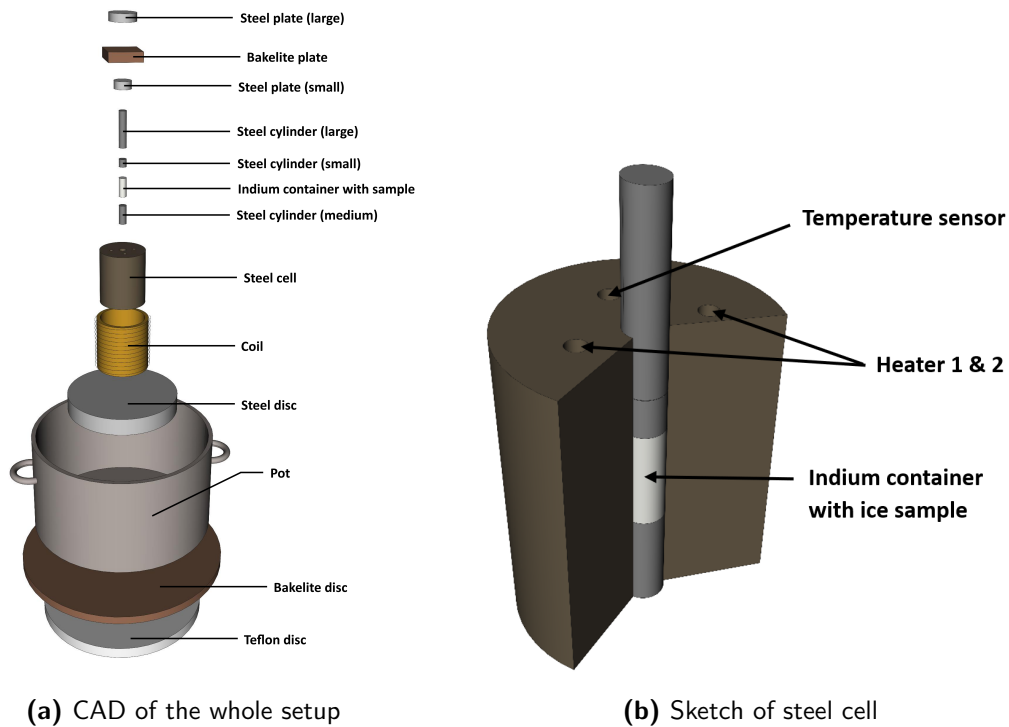
Figure 5: Sketch of the implemented piston-cylinder setup

The sample pressure p can be calculated from the applied force F and the radius $r = 4\,\text{mm}$ of the used steel cell as

$$p = \frac{F}{A} = \frac{F}{\pi r^2}$$

and is tabulated for some notable values in Table 2.

Each sample is labelled as *SHxx* (with *xx* being a number), which makes it easier to assign the diffractograms to their respective sample.

| Force [kN]	Pressure [GPa]
1	0.02
3	0.06
10	0.20
25	0.50
40	0.80
55	1.09
80	1.59
90	1.79

Table 2: Resulting sample pressure for applied force for cell with $8\,\text{mm}$ diameter

3.2   X-ray diffraction

X-ray diffraction (XRD) is a useful method to investigate the structure of materials. In the case of an ideal single crystal, interference occurs due to the scattering of X-rays at neighboring lattice planes. The scattering angle 2θ of the high-intensity reflexes is given by Bragg's law

$$2 \cdot d_{hkl} \cdot \sin\left(\theta\right) = n\lambda$$

which can be derived from geometric considerations, shown in Figure 6. The path difference between the two coherent beams is $2 \cdot d_{hkl} \cdot \sin\left(\theta\right)$ and should be an integer multiple n of the used wavelength λ. Here, $d_{hkl} = \frac{g}{\sqrt{h^2+k^2+l^2}}$ is the distance between lattice planes, described by the Miller indices (hkl) and g being the lattice constant.
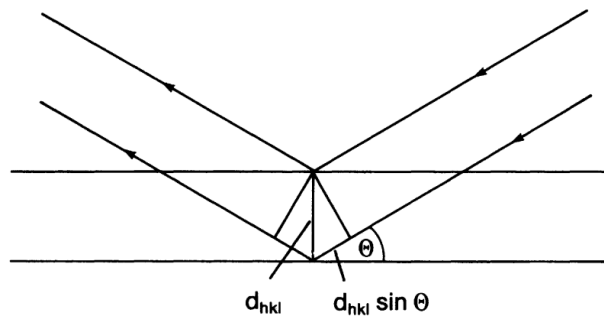
**Figure 6:** Derivation of Bragg's law. (Adapted from ref. [31])

Since samples are rarely available as single crystals, powder diffraction is often employed in laboratories instead. In this technique, the sample ideally consists of numerous small crystallites that are randomly oriented.

(a) Crystalline   **(b)** Amorphous
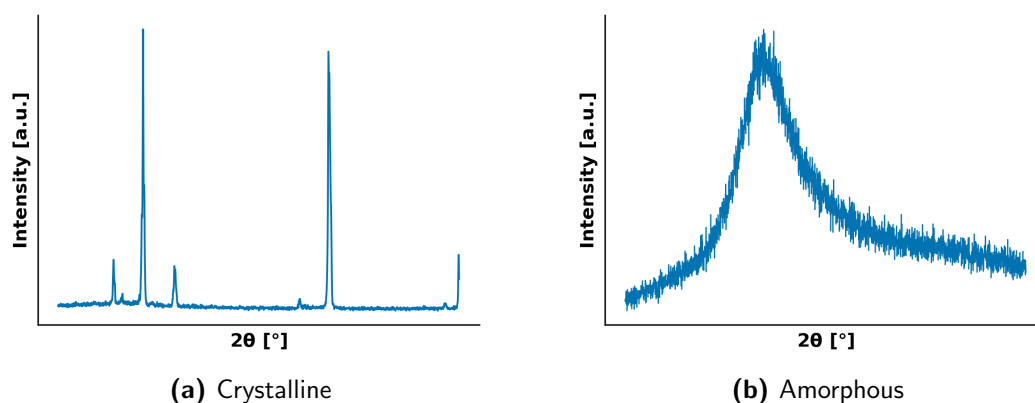
Figure 7: Schematic illustration of the difference in the XRD measurements for a **(a)** crystalline and **(b)** amorphous sample

Furthermore, Figure 7 illustrates the difference between diffractograms for crystalline and amorphous substances. For a crystalline substance, the periodic lattice structure manifests as sharp peaks in the diffraction pattern. An amorphous substance in contrast exhibits a much broader diffraction maximum due to the lack of long-range order.

To characterize the structure of the samples, powder X-ray diffraction measurements are done, using the Rigaku SmartLab diffractometer (Figure 8a). For the measurement, a rotating copper anode is used, so the main peak of the used X-ray spectrum consists of the K_{α_1}-line of copper ($\lambda_{K_{\alpha_1}} = 1.540\,59$ Å). Since for characterization of amorphous sample, one studies the rather broad first diffraction maximum, a lower resolution resulting from the additional low-intensity K_{α_2}- and K_{β}-line of the copper anode are not much of a disruptive factor.

(a) Rigaku SmartLab   **(b)** Anton Paar TTK 600
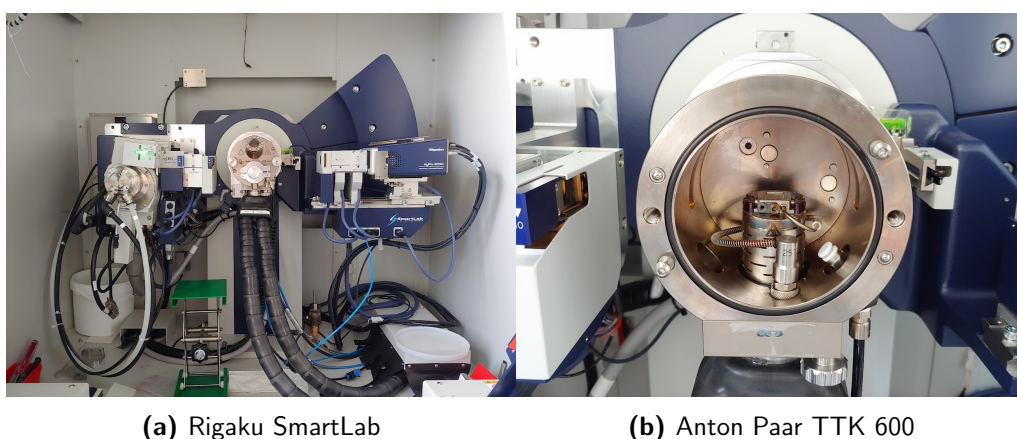
Figure 8: X-ray diffractometer with low-temperature chamber

The measurement is done in the so-called $\theta - \theta$ geometry (Figure 9), which means X-ray source and detector (HyPix-3000) are mounted onto goniometer arms and are

simultaneously moved by an angle θ in opposite direction to each other.
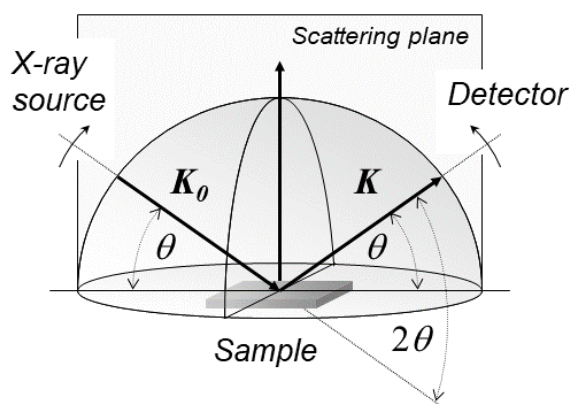
Figure 9: $\theta - \theta$ geometry (Taken from ref. [32])

There are several challenges associated with conducting XRD measurements of metastable ice samples. Above $\sim 130\,\mathrm{K}$, uHDA and VHDA transform into LDA, and at even higher temperatures, LDA starts to crystallize into cubic ice ($\mathrm{I_c}$), which further transforms into hexagonal ice ($\mathrm{I_h}$).

To overcome these challenges, the ice samples need to be kept at around $77\,\mathrm{K}$ during preparation and installation in the low-temperature chamber, Anton Paar TTK 300 (Figure 8b).

This is achieved by preparing the samples in a styrofoam box filled with liquid nitrogen and adequately cooling the tools used for preparing before coming into contact with the ice sample or the indium container. The retrieved samples are ground into a powder and to prevent crystallization during the XRD measurement, they are transferred to the low-temperature chamber, which is cooled with liquid nitrogen to approximately $83\,\mathrm{K}$ using an Anton Paar CCU 100 device.

Also, a vacuum pump (Vacuubrand MV 2 VARIO select) is used to achieve a pressure of about $1\,\mathrm{mbar}$ inside the chamber.

Before starting the measurement, an optical and a sample alignment are done. The measurement is performed for scattering angles 2θ in the range of $10°$ to $50°$ in steps of $0.01°$ with a speed of $5\,°/\mathrm{min}$ in the 1D scanning mode.

Since the measured intensity in an XRD measurement depends on the amount of sample, the reported intensity, even though it is stated as counts per second (cps), is arbitrary as it does not account for the quantity of the sample transferred which likely differs for each measurement.

3.3   Making the aqueous solutions

In order to make a solution of a given mole fraction $\chi = \frac{n_\mathrm{s}}{n_\mathrm{s}+n_{\mathrm{H_2O}}}$, the volume V_s or weight m_s of substances (with molar weight M_s and mass density ρ_s) one needs to add to a volume $V_{\mathrm{H_2O}}$ of water with molar mass[33] $M_{\mathrm{H_2O}} = 18.015\,\mathrm{g/mol}$ and mass density[34] $\rho_{\mathrm{H_2O}} = 0.9982\,\mathrm{g/mL}$ at room temperature can be calculated via the following formulas:

$$V_\mathrm{s} = \frac{\chi}{1-\chi} \cdot \frac{M_\mathrm{s}}{M_{\mathrm{H_2O}}} \cdot \frac{\rho_{\mathrm{H_2O}}}{\rho_\mathrm{s}} \cdot V_{\mathrm{H_2O}}$$

$$m_\mathrm{s} = \frac{\chi}{1-\chi} \cdot \frac{M_\mathrm{s}}{M_{\mathrm{H_2O}}} \cdot \rho_{\mathrm{H_2O}} \cdot V_{\mathrm{H_2O}}$$

For each substance (glycerol, sorbitol, erythritol), two solutions are prepared, one with mole fraction $\chi = 0.02$ and one with $\chi = 0.10$.

All solutions are made using (10.000 ± 0.025) mL Milli-Q water, measured with a volumetric flask. In Table 3 the different investigated samples are listed together with the given information.

Substance	Manufacturer	Purity	Molar mass [g/mol]	Density [g/mL]
Glycerol	Sigma-Aldrich	$\geq 99.5\,\%$	92.09	1.25
Sorbitol	Fisher Scientific	$\geq 97\,\%$	182.17	1.49[35]
Erythritol	Jungbunzlauer	-	122.12[36]	1.45[36]

Table 3: Investigated substances, their molar mass and density

For the glycerol solutions, the calculated volume of glycerol needed, as well as the measured volume can be found in Table 4. A syringe is needed due to the high viscosity of glycerol. Otherwise, there would be leftovers within the pipette, making the volume measurement imprecise.

For the sorbitol and erythritol solutions, a scale with an accuracy of $10^{-4}\,\mathrm{g}$ was used to weigh the amount needed for the solutions, since they are powder samples. The calculated and measured mass for these solutions is listed in Table 4 as well.

Substance	Mole fraction χ	Calculated	Measured
Glycerol	0.02	0.833 mL	(0.84 ± 0.01) mL
	0.10	4.536 mL	(4.6 ± 0.2) mL
Sorbitol	0.02	2.0560 g	(2.0560 ± 0.0001) g
	0.10	11.2155 g	(11.2156 ± 0.0001) g
Erythritol	0.02	1.3809 g	(1.3809 ± 0.0001) g
	0.10	7.5184 g	(7.5189 ± 0.0001) g

**Table 4:** Calculated and measured volume/mass for the solutions

4 Data analysis

4.1 Amorphous transitions of water

4.1.1 uHDA

To make amorphous ices via pressure-induced amorphization (PIA), one has to make unannealed high-density amorphous ice (uHDA) first. So the first step for making the amorphous ice samples is by compressing ice I_h at about $77\,\mathrm{K}$ from ambient pressure to about $1.59\,\mathrm{GPa}$.

Before this final compression run, three pre-compression runs (up to 0.06, 0.20 and $0.50\,\mathrm{GPa}$) in increasing order are done, to reduce air pockets and mechanical effects caused by the setup. Later, starting from sample SH15, only the third pre-compression run is done. The different pre-compression runs are shown in Figure 10, where the applied pressure is plotted against the piston displacement which is proportional to the density of the sample.
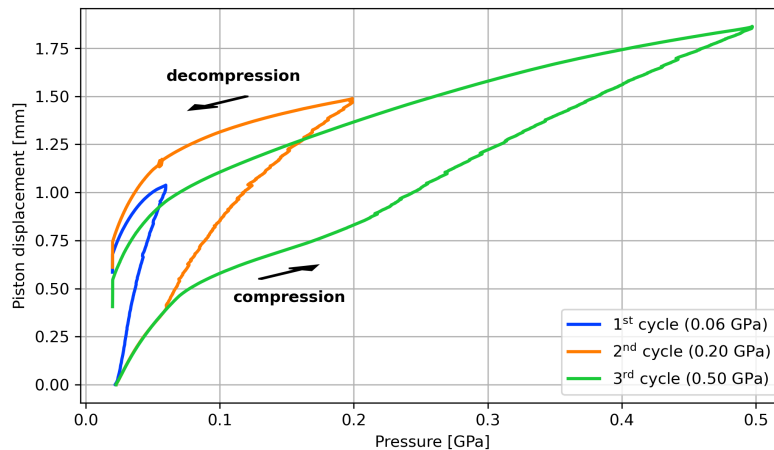
Figure 10: Pre-compression runs of ice I_h at $\sim 78\,\mathrm{K}$ (SH05)

The final compression run (Figure 11) shows an abrupt change in the piston displacement and therefore in the density of the sample. To determine the density of the sample, the piston displacement needs to be corrected due to volume changes resulting from the setup and not from the sample. This can be done by doing the compression/decompression cycle without the ice sample, shown as the dotted line in Figure 11. This compression and decompression curves are then interpolated using a spline interpolation of order $k = 5$ and then subtracted from the data with an ice sample. The resulting compression and decompression curves are plotted in Figure 12.
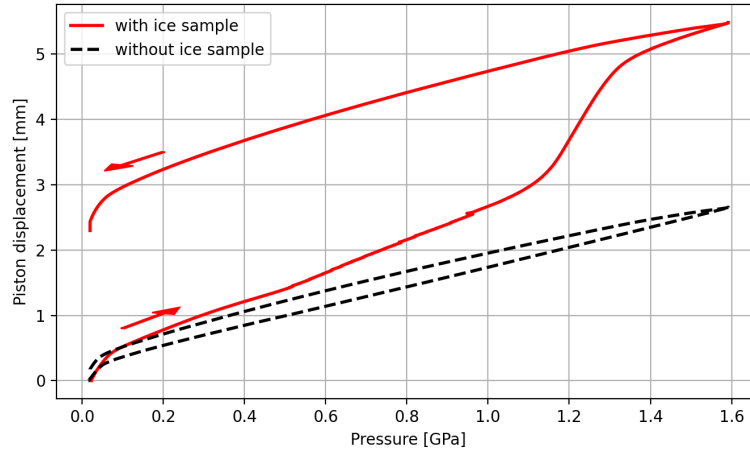
Figure 11: Final compression run of ice I_h (red line) at $78\,\text{K}$ and same cycle without the ice sample (dotted line)
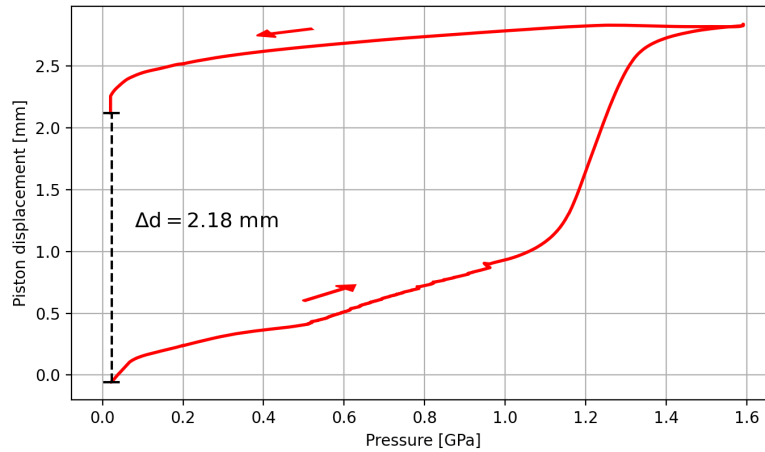
Figure 12: Corrected piston displacement for the final compression run by subtracting the interpolated piston displacement without ice sample

From the difference $\Delta d = 2.18\,\text{mm}$ between the corrected piston displacement before the compression and after the decompression, the density ρ_uHDA change can be calculated by assuming that the mass of the sample stays the same after cooling and compressing:

$$m = \rho_{20\,°\text{C}} \cdot V_{20\,°\text{C}} = \rho_\text{uHDA} \cdot V_\text{uHDA} = \rho_{I_h} \cdot V_{I_h}$$

By using $V_\text{uHDA} = V_{I_h} - A \cdot \Delta d$ with $A = \pi r^2$, estimating the radius of the cell as $r = 3.8\,\text{mm}$ since the indium foil has a thickness of $0.2\,\text{mm}$ and using the literature values[34,37] for the densities $\rho_{20\,°\text{C}} = 0.9982\,\text{g/cm}^3$ and $\rho_{I_h} = 0.9348\,\text{g/cm}^3$ at ambient pressure for a temperature of $20\,°\text{C}$ and $-180\,°\text{C}$ respectively, the density of uHDA is

calculated to be

$$\rho_{\mathrm{uHDA}} = \frac{\rho_{20\,^\circ\mathsf{C}} \cdot V_{20\,^\circ\mathsf{C}}}{V_{\mathrm{I_h}} - A \cdot \Delta d} = \frac{\rho_{20\,^\circ\mathsf{C}} \cdot V_{20\,^\circ\mathsf{C}}}{\frac{\rho_{20\,^\circ\mathsf{C}}}{\rho_{\mathrm{I_h}}} \cdot V_{20\,^\circ\mathsf{C}} - \pi r^2 \cdot \Delta d} = (1.22 \pm 0.02)\,\mathsf{g/cm^3}$$

The error is calculated using Gaussian error propagation and estimating an error in the last given digit.

Compared to the reported value in literature[18] of $\rho_{\mathrm{uHDA}} = 1.15\,\mathsf{g/cm^3}$, the result deviates upwards by $6.09\,\%$. This considerable deviation indicates a systematic error which could be due to e.g. irreversible compression of some parts of the setup like the indium container or the steel plates during the final compression run compared to the run without the ice sample, as the steel plates show notches from previous measurements.

4.1.2 VHDA

By annealing uHDA at a pressure of about $1.09\,\mathsf{GPa}$, its density increases. However, since there is thermal expansion of the material itself, the decrease in volume is not observed directly during compression. The decrease in volume, hence total densification, is evident if one quenches the sample after the heating process at the same pressure, shown in Figure 13.

The sample SH08 shows the expected shape of the curve[21], while sample SH04 has a kink during the annealing from $\sim 130\,\mathsf{K}$ to $\sim 150\,\mathsf{K}$. This could be caused by heating effects due to friction within the cell which occurs from time to time with a characteristic cracking sound and kinks in the piston displacement curve.
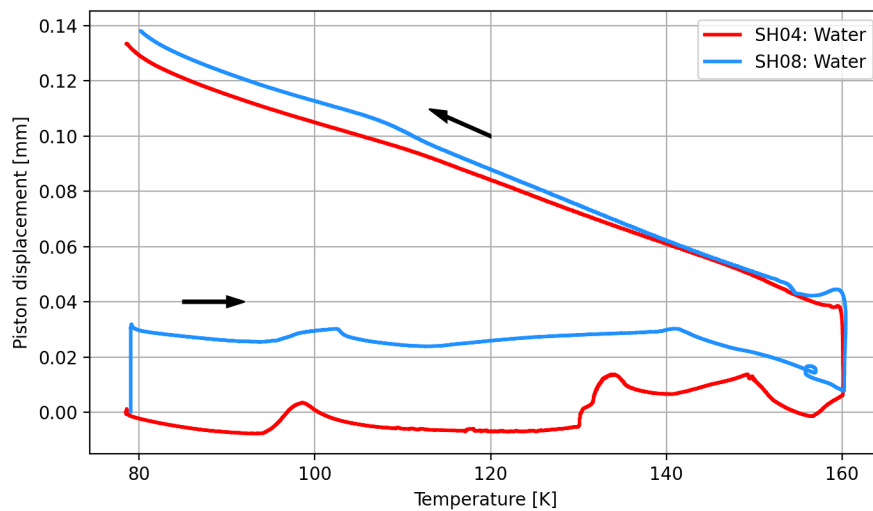

Figure 13: By annealing uHDA to $160\,\mathsf{K}$ and subsequent quenching at $1.1\,\mathsf{GPa}$ an increase in density is observed

The diffractogram (Figure 14) shows a broad amorphous maximum at $\sim 32°$ (see red dashed line) indicating its lack of long-range order. The position of this amorphous peak was determined by fitting a Voigt function with a linear background to it and is in agreement with the expected location from the literature.[18] The fitting parameters can be found in the appendix (Table 8).

The sharp Bragg reflex at $\sim 44.5°$ (indicated by a gray star) results from the sample holder, as a background measurement of the empty low-temperature chamber (appendix, Figure 35) and its manual, both indicating nickel as the material of the sample holder[38], suggest.

The very low intensity of the amorphous peak can be explained by the low amount of powder which could be transferred to the sample holder.
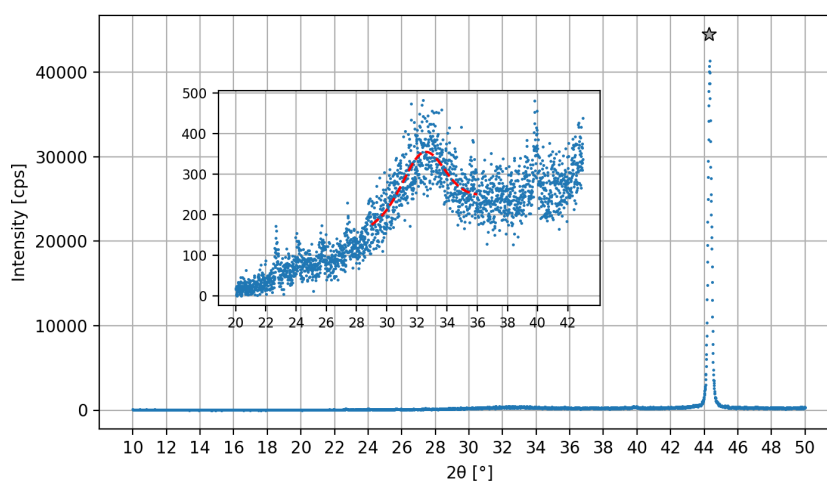
Figure 14: XRD measurement of the VHDA sample (SH04). The red dashed line indicates the amorphous maximum at $\sim 32°$. The gray star marks the Bragg reflex from the sample holder.

4.1.3 LDA

There are two ways to make LDA. One way is by annealing uHDA up to about $140\,\mathrm{K}$ at ambient pressure.[14,15] LDA made this way is also named LDA-I. In Figure 15 one can see the rapid increase in volume upon heating uHDA at $0.02\,\mathrm{GPa}$.

Another way to make so-called LDA-II is by decompressing VHDA at about $140\,\mathrm{K}$.[15–17]
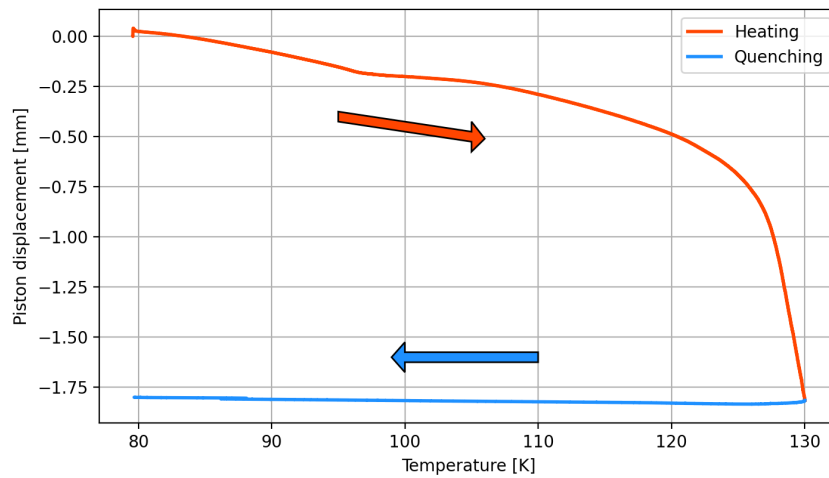
Figure 15: Annealing uHDA to $140\,\text{K}$ and subsequent quenching at $0.02\,\text{GPa}$ (SH05). A decrease in density is observed upon heating, indicating the transition to LDA.
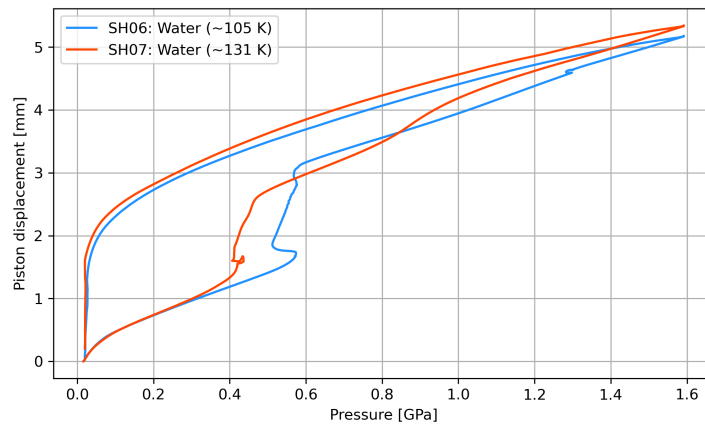
Figure 16 shows the XRD measurement of the LDA sample. An amorphous maximum at about $24°$ is evident (see red dashed line), which is in accordance with the reported value in literature.[16] However, there are also Bragg reflexes from hexagonal ice (I_h) at $22.7°$, $24.3°$, $25.8°$, $33.4°$ and $40.0°$ (marked by blue hexagons)[39], presumably resulting due to condensation of water vapour from air during the preparation of the sample for the XRD measurement. Also maybe peaks from cubic ice (I_c) at $24.3°$ and $40.0°$ (marked by blue squares) resulting from crystallization of LDA, as well as the peak from the sample holder are observed.
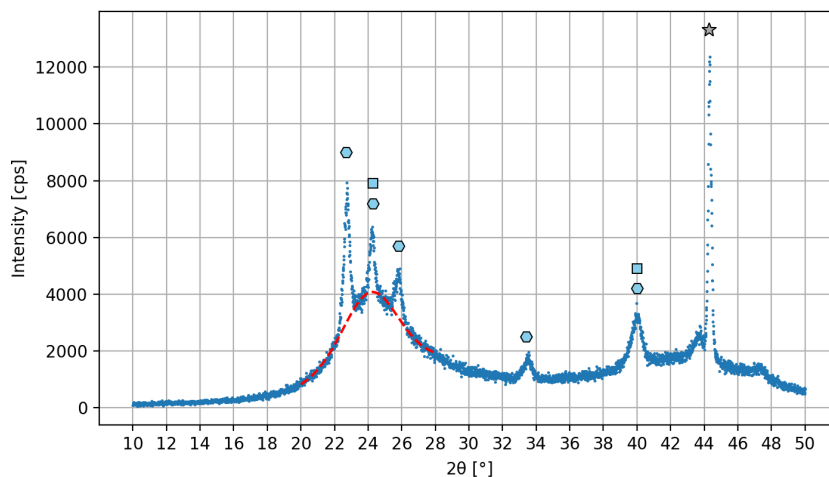
Figure 16: XRD measurement of the LDA sample (SH05). The red dashed line indicates the amorphous maximum at $\sim 24°$ resulting from LDA. Blue hexagons and squares respectively mark the Bragg reflexes of hexagonal and cubic ice.

4.1.4   LDA $\leftrightarrow$ HDA

If one compresses LDA at temperatures below $\sim 140\,\text{K}$, a sudden increase in density is observed (Figure 17). The onset-pressure for this transition decreases from $\sim 0.6\,\text{GPa}$ to $\sim 0.4\,\text{GPa}$ with increasing temperature, as expected from the narrower hysteresis in the literature.[20]. Both samples are decompressed at $\sim 140\,\text{K}$ in order to observe the transition back to LDA.

Figure 17: LDA $\leftrightarrow$ HDA transition for pure water: Compression is done at $\sim 105\,\text{K}$ and $\sim$ 131 K respectively, while decompression is done at $\sim 140\,\text{K}$ for both samples.

The XRD measurement of the sample (Figure 18) shows a broad first diffraction maximum at $\sim 24°$ similar to the LDA sample made by annealing uHDA to $\sim 140\,\text{K}$, thus suggesting the sample being LDA. The rather distinct Bragg peaks at $\sim 24°$ and $\sim 40°$ are most likely due to cubic ice (I_c), since LDA first crystallizes to ice I_c before further transforming to hexagonal ice (I_h).[3]
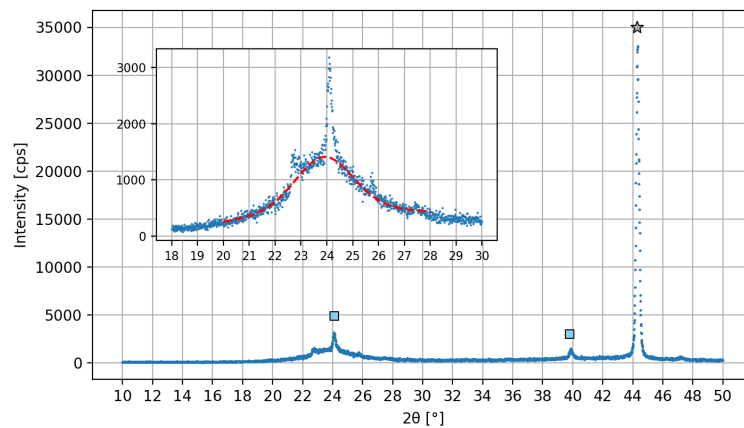
Figure 18: XRD measurement of the sample SH07. The red dashed line shows an amorphous maximum at $\sim 24°$.

4.2   Glycerol solutions

### 4.2.1   Amorphous transitions in glycerol solutions

uHDA

The different amorphous transitions of water are also observed for the prepared glycerol solutions. The uHDA transitions for the 0.02 and 0.10 mf solutions upon compressing the sample at ~ 77 K is shown in Figure 19.

As indicated by the dotted lines, the onset-pressure increases for increasing concentration, as one would expect based on previous experimental results.[30]

The onset-pressures are determined by fitting two linear curves for ranges before and immediately after the transition and determining the intersection point of these two curves. The resulting fit parameters and onset-pressures are listed in Table 6.

Likewise, the transition happens over a larger pressure range for the higher concentrated solution, as it was pointed out in the same study.[30]

For sample SH10 it was not clear if a compression to 1.59 GPa was enough for a full transition to uHDA of the 0.10 mf solution. So for the sample SH14 with the same concentration the compression was done up to a pressure of 1.79 GPa where a decrease in slope after the transition is observable, indicating the complete transition to uHDA.
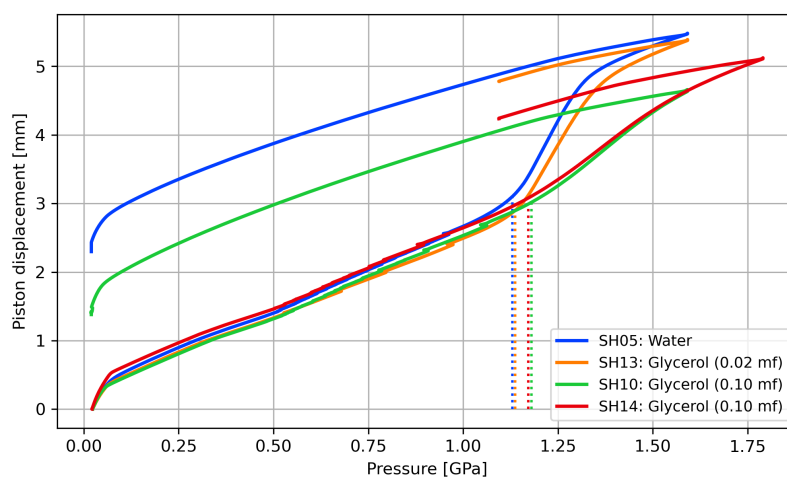
Figure 19: Compressing glycerol solutions of different mole fractions at 78 K indicating the uHDA transition

The XRD measurement of the sample SH10 is plotted in Figure 20. At first glance, it seems like a very broad peak at $\sim 26°$ but it can be interpreted as a combination of a maximum at $\sim 28°$ resulting from uHDA and one at $\sim 24°$ possibly resulting from LDA due to heat-induced transformation of some part of the uHDA sample during transferring or preparing it for the XRD measurement.
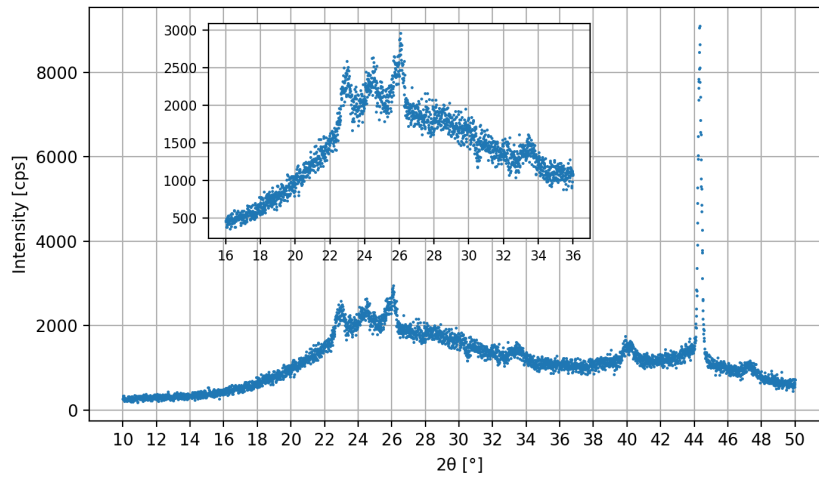
Figure 20: XRD measurement of the sample SH10. A broad maximum ranging from $20°$ to $30°$ can be interpreted as two maxima at $\sim 24°$ and $\sim 28°$ overlapping.

VHDA

By annealing and subsequent quenching the prepared uHDA samples at $1.09\,\text{GPa}$, one can see an increase in density (Figure 21). While the piston displacement curve for the $0.02\,\text{mf}$ solution shows a similar course as the pure water sample, it seems like the VHDA transition for the $0.10\,\text{mf}$ solution occurs at lower temperatures ($\sim 150\,\text{K}$ compared to $\sim 160\,\text{K}$ for pure water) with a larger change in piston displacement during annealing.
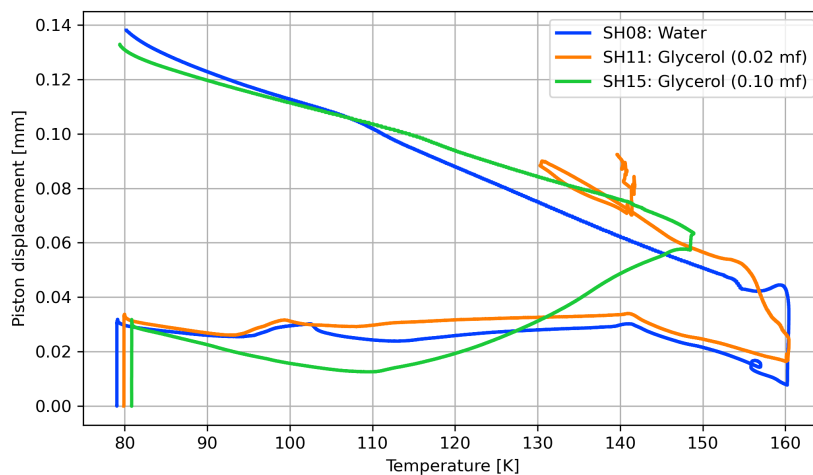
Figure 21: Annealing and subsequent quenching uHDA samples made from glycerol solutions of different mole fractions at $1.09\,\text{GPa}$ indicating the transition to VHDA

Figure 22 shows the annealing of a uHDA sample (SH12) made from the $0.10\,\text{mf}$ solution. One can see a much larger piston displacement compared to the $0.10\,\text{mf}$ sample (SH15) in Figure 21.

The difference between the samples SH12 and SH15 is that for SH12 the uHDA sample made by compression to 1.59 GPa at ~ 79 K was fully decompressed to 0.02 GPa, then recompressed to 1.09 GPa and finally annealed to ~ 160 K. For the sample SH15 however, the uHDA made by compression to 1.59 GPa at ~ 79 K was directly decompressed to 0.02 GPa. This discrepancy due to the sample's history is a known phenomenon in literature.[21]
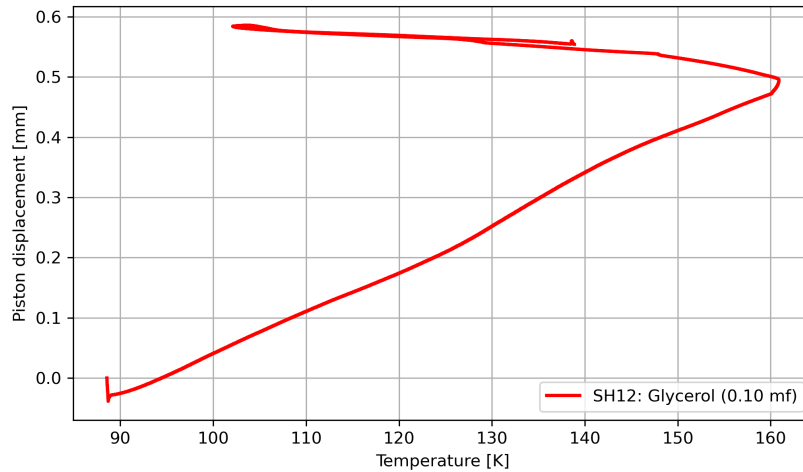

Figure 22: Annealing and subsequent quenching uHDA made from a 0.10 mf glycerol solution at 1.09 GPa. The uHDA sample was first decompressed to 0.02 GPa before recompressing it to 1.09 GPa.

LDA $\leftrightarrow$ HDA

Instead of annealing uHDA to ~ 140 K at ambient pressure, LDA samples for all further measurements are prepared by decompressing VHDA from 1.09 GPa to 0.02 GPa at ~ 140 K as shown in the appendix (Figure 36).

Upon compression of the LDA sample (Figure 23) the LDA $\leftrightarrow$ HDA transition could be observed for the both concentrations at a temperature of ~ 140 K with an onset-pressure of ~ 0.39 GPa for the 0.02 mf sample and ~ 0.43 GPa for the 0.10 mf sample. The onset-pressure for this transition was determined similarly to the case of the uHDA transition. The fitted parameters for each sample can be found in the appendix (Table 7) as well.

Furthermore, just as for the uHDA transition, the transition becomes gradually continuous for increasing amount of glycerol, as one can see the from the higher slope for the 0.02 mf sample compared to the 0.10 mf sample, for which the transition happens over a wider pressure range as well.
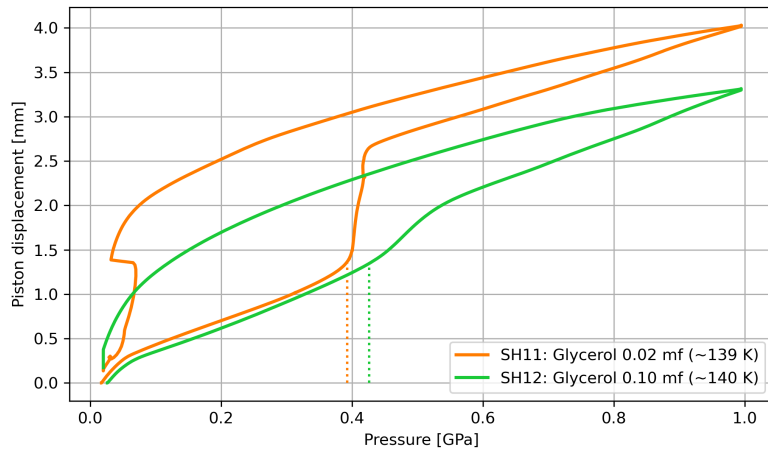
Figure 23: Compression and subsequent decompression of LDA samples made from $0.02\,\text{mf}$ and $0.10\,\text{mf}$ glycerol-water solutions at $\sim 140\,\text{K}$. The dotted lines mark the position of the determined onset-pressures.

For temperatures above $140\,\text{K}$ an increase in density can be observed for both concentrations as well (Figure 24). However, the onset-pressures for this transition range from $0.66\,\text{GPa}$ to $0.68\,\text{GPa}$, so abruptly becoming higher compared to the LDA $\leftrightarrow$ HDA transition at $T \lesssim 140\,\text{K}$ which contradicts the expectation of a shift to lower onset-pressures for increasing temperatures from literature.[27,28]

This indicates that a different transition rather than the LDA $\rightarrow$ HDA transition takes place upon compressing the glycerol samples at $T > 140\,\text{K}$.

(a)   (b)
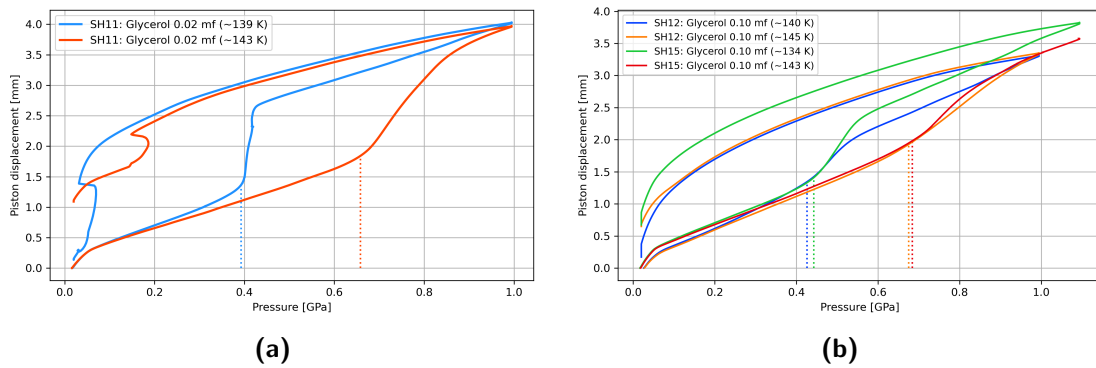
Figure 24: Compression and subsequent decompression of the **(a)** $0.02\,\text{mf}$ and **(b)** $0.10\,\text{mf}$ LDA samples for different temperatures. The dotted lines mark the position of the onset-pressures for transitions leading to densification.

This assumption is further verified by the XRD measurements (Figure 25) showing distinct Bragg reflexes at $22.9°$, $26.6°$, $29.9°$ and $32.7°$.

After a comparison with the literature[40], it is found that the observed diffractograms likely represent ice IX.
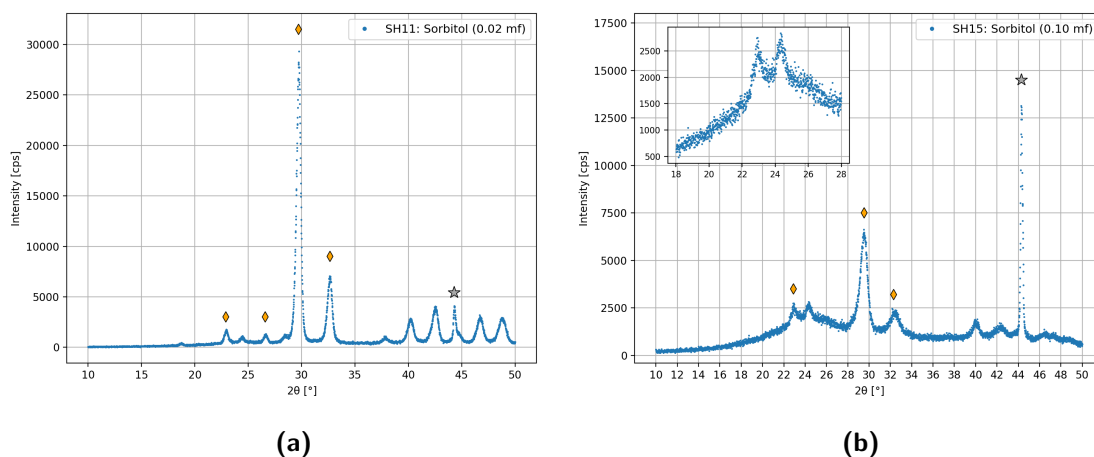
Figure 25: XRD measurement of the sample **(a)** SH11 and **(b)** SH15. The orange rhombuses mark the position of peaks from ice IX.

### 4.2.2   X-ray study of glycerol and glycerol solutions

To study the structure of the glycerol solutions at low temperatures, a measurement series is done, in which the X-ray diffractograms of water, glycerol and the 0.10 mf glycerol solution are recorded.

Pure glycerol

A glass capillary was filled with pure glycerol using a syringe and then placed inside the low-temperature chamber. The settings for the XRD measurement were the same as for the powder measurements (see subsection 3.2). Then XRD measurements were performed for different temperatures by cooling the chamber from 300 K to 83 K. The resulting diffractograms are shown in Figure 26. One can see a broad maximum between $20°$ and $21°$ for all temperatures.

To determine the position of the centre (indicated by the dashed lines), a Voigt function with a linear background was fitted to the data. The fitted parameters can be found in the appendix (Table 8). It is evident, that the position of the maximum shifts to higher scattering angles upon cooling the sample down to 148 K.

Further cooling of the sample does not show such an effect. This can be interpreted by noting that the glass transition temperature of glycerol is at about 190 K[41], indicating that for liquid glycerol, the local order changes much more than for the glassy state below 190 K.
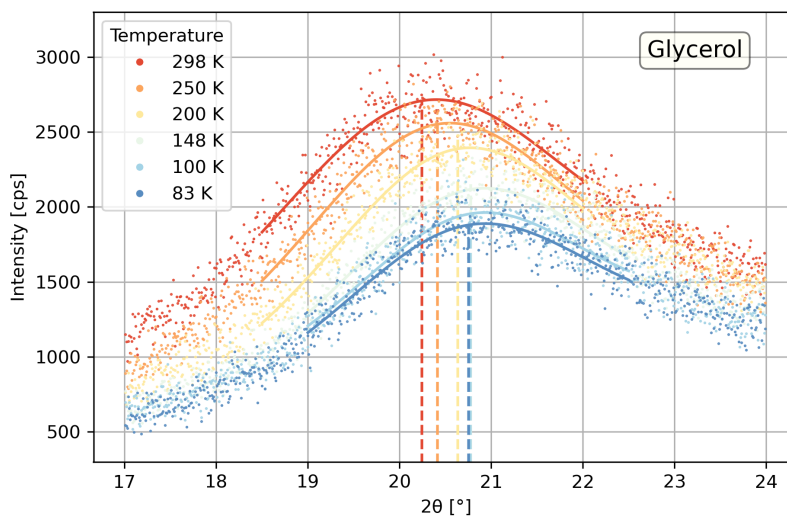
Figure 26: XRD measurements of pure glycerol sample upon cooling from $298\,\mathrm{K}$ to $83\,\mathrm{K}$

Water and glycerol solution (0.10 mf)

| (a) | (b) |
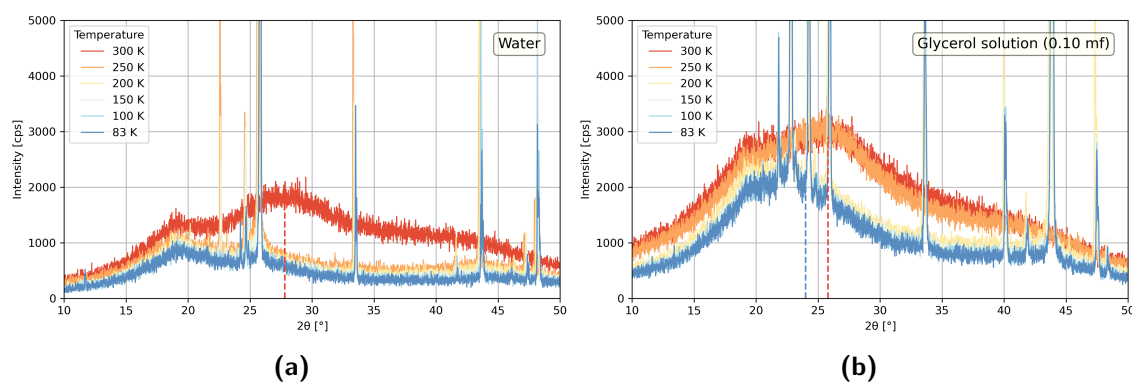
Figure 27: XRD measurement of **(a)** pure water and **(b)** glycerol solution $(0.10\,\mathrm{mf})$ upon cooling from $300\,\mathrm{K}$ to $83\,\mathrm{K}$

Similar XRD measurements were performed for pure water and the $0.10\,\mathrm{mf}$ glycerol solutions and are shown in Figure 27.

The only difference in the procedure compared to the measurement of the pure glycerol sample was that Kapton capillaries were used instead of glass due to the possibility of the glass shattering upon cooling. The specifications of the Kapton capillary (Table 9) as well as a background measurement (Figure 37) can be found in the appendix.

For liquid water (Figure 27a) at $300\,\mathrm{K}$, an amorphous maximum is present $\sim 28°$, indicated by a red dashed line. Another maximum can be observed at $\sim 19°$ for all temperatures and is due to the Kapton capillary, as the measurement with an empty

capillary suggest. The pure water crystallizes upon cooling, leading to Bragg reflexes of hexagonal ice (I_h).

For the 0.10 mf glycerol solution (Figure 27b), an amorphous maximum at $\sim 26°$ (indicated by the red dashed line) is evident at 300 K and 250 K. Also, the lack of Bragg reflexes shows that the sample is still liquid at 250 K as compared to the pure water sample.

Upon further cooling, Bragg reflexes are observed, indicating crystallization takes place. However, there is still an amorphous maximum present at $\sim 24°$, indicated by a blue dashed line. By considering the interpretation suggested by Bachler et al.[30], this could indicate the phase separation of the sample into maximally freeze-concentrated solution (MFCS) and hexagonal ice (I_h) domains upon cooling, since the position of the amorphous maximum seems to shift with the concentration of the sample, i.e. from pure liquid water: $\sim 28° \rightarrow 0.10$ mf glycerol solution: $\sim 26° \rightarrow$ MFCS: $\sim 24° \rightarrow$ pure glycerol: $\sim 20°$.

4.3   Sorbitol solutions

uHDA

Similar to pure water and the glycerol solutions, also for the 0.02 mf sorbitol solution, the transition to uHDA upon compression up to 1.79 GPa at a temperature of 77 K could be observed (Figure 28). A higher onset-pressure of 1.20 GPa as compared to 1.13 GPa for pure water is in accordance with the previous observation of an increasing onset-pressure for higher mole fractions.

In the case of the 0.10 mf, there is no clear onset-pressure evident, perhaps indicating that for sorbitol solutions with concentrations of $\gtrsim 0.10$ mf the transformation has broadened so much that the final pressure of 1.79 GPa is too low for a complete transition to uHDA. A similar result has been reported for glycerol solutions with concentrations $\gtrsim 0.20$ mf.[30]
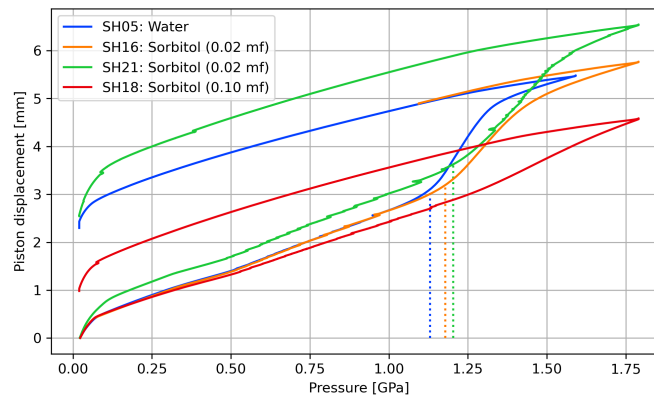
Figure 28: uHDA transition of sorbitol solutions for different mole fractions upon compression to 1.79 GPa. The dashed lines indicate the onset-pressure for the transition.

As indicated by the dashed lines, the lack of an amorphous maximum at $\sim 28°$ in the XRD measurement (Figure 29) of the $0.10\,$mf sample as compared to the $0.02\,$mf sample further suggests the absence of the uHDA transition of the $0.10\,$mf sample.
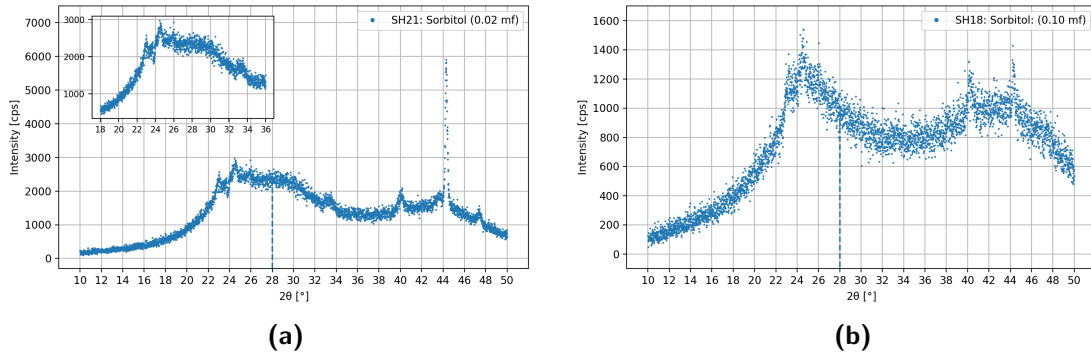

Figure 29: XRD measurement of the sample **(a)** SH21: Sorbitol $(0.02\,$mf$)$ and **(b)** SH18: Sorbitol $(0.10\,$mf$)$. A dashed line at $\sim 28°$ marks the position for the maximum of an expected uHDA sample which is only observed for the SH21 sample.

LDA ↔ HDA transition

The annealing of the uHDA samples of different mole fractions at $1.59\,$GPa is plotted in the appendix (Figure 38) together with their XRD measurements (Figure 39). Some notable findings are that the VHDA transition seems to occur at about $148\,$K instead of $160\,$K as for the pure water sample. In contrast to $0.10\,$mf sample, the XRD measurement of the $0.02\,$mf sample shows a broad amorphous maximum at $\sim 32°$, as one would expect. Since due to the lack of the uHDA transition for the $0.10\,$mf solution, there also should not be a VHDA transition for this sample.

LDA samples of the $0.02\,$mf solution were then prepared by decompressing the VHDA sample at $140\,$K from $1.09\,$GPa to $0.02\,$GPa.

The compression and subsequent decompression of these LDA samples is plotted in Figure 30a. As indicated by the dotted lines, one can see how the onset-pressure for LDA $\rightarrow$ HDA transition shifts from $0.42\,$GPa at $125\,$K to $0.37\,$GPa at $142\,$K. This is in accordance with the previous observation for pure water, where the onset-pressure shifted to lower values for increasing temperatures. Also, the HDA sample for the compression at $125\,$K does not transform back to LDA, in contrast to the decompression of the HDA sample at $142\,$K. Only upon heating at $0.02\,$GPa from $125\,$K to $140\,$K the HDA sample undergoes transition to LDA, as one can see from the rapid decrease in density (Figure 30b) and the XRD measurement (Figure 31a) showing a broad maximum at $\sim 24°$.
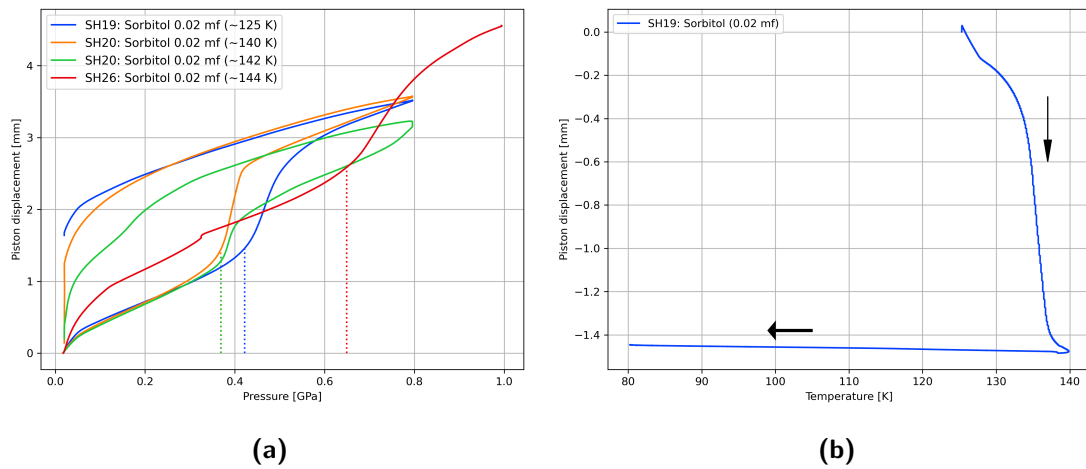
Figure 30: **(a)** Compression of LDA made from sorbitol-water ($0.02\,\text{mf}$) at different temperatures (dotted lines indicate the onset-pressure of rapid densificaton) and **(b)** Annealing the HDA state of the SH19 sample from $125\,\text{K}$ to $140\,\text{K}$
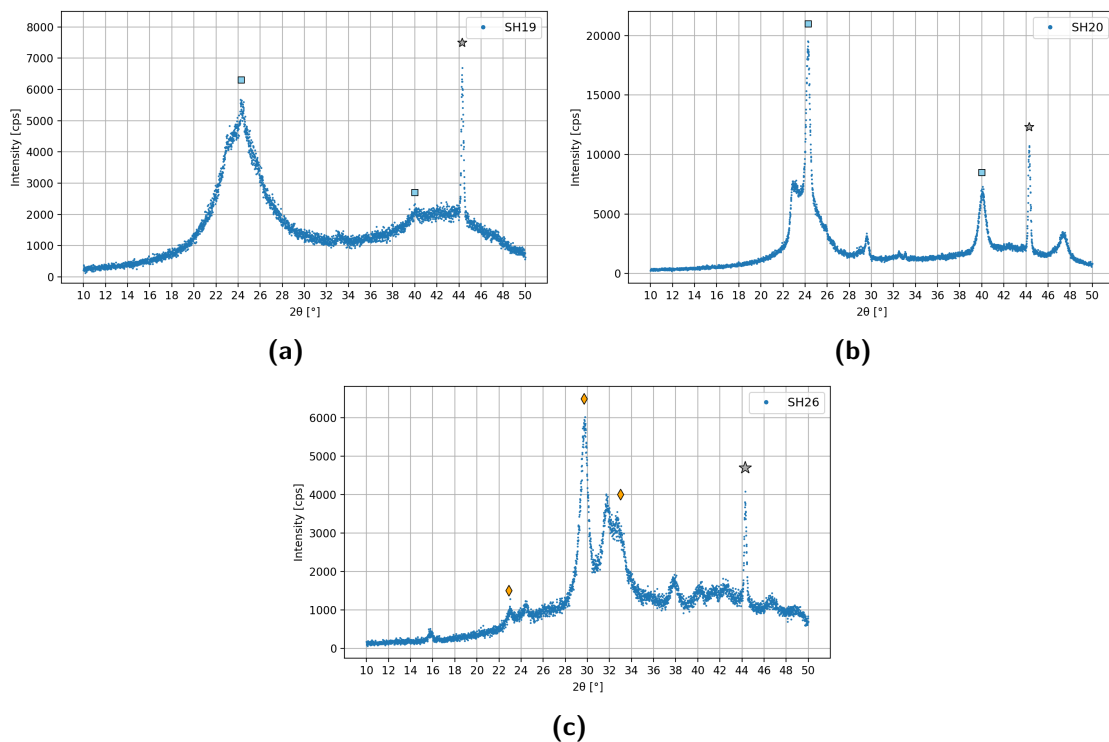
Figure 31: XRD measurement of the samples **(a)** SH19: Sorbitol ($0.02\,\text{mf}$, $\sim 125\,\text{K}$), **(b)** SH20: Sorbitol ($0.02\,\text{mf}$, $\sim 142\,\text{K}$) and **(c)** SH21: Sorbitol ($0.02\,\text{mf}$, $\sim 145\,\text{K}$). SH19 and SH20 show an amorphous maximum at $\sim 24°$ indicating LDA and began to crystallize to ice I_c. SH26 shows Bragg reflexes of ice IX indicating it underwent pressure-induced crystallization instead of transforming to HDA

These two observations verify that the hysteresis of the LDA $\leftrightarrow$ HDA transition becomes narrower for the solution up to $T \approx 142\,\text{K}$.

However, for the compression at $144\,\mathrm{K}$ the onset-pressure of a transition leading to densification shifts to $0.65\,\mathrm{GPa}$. This abrupt increase of the onset-pressure is similar as for the glycerol solutions, which transformed to ice IX upon compression at $T > 140\,\mathrm{K}$. In the case of the $0.02\,\mathrm{mf}$ sorbitol solution, the XRD measurement (Figure 31c) shows the characteristic peaks of ice IX as well, hence it also undergoes pressure-induced crystallization instead of transforming to HDA.

4.4   Erythritol solutions

An erythritol solution with a concentration of $0.10\,\mathrm{mf}$ could not be prepared because a considerable amount of erythritol sedimented. So only the $0.02\,\mathrm{mf}$ solution could be studied.

uHDA

The compression of the solution cooled at $78\,\mathrm{K}$ is shown in Figure 32a and shows a similar increase of the onset-pressure from $1.13\,\mathrm{GPa}$ to $1.20\,\mathrm{GPa}$ compared to water. This is equal to the shift of the $0.02\,\mathrm{mf}$ sorbitol solution.

The XRD measurement of the sample Figure 32b only shows a broad maximum at $\sim 24°$ which may come from heat-induced transition of uHDA to LDA during transferring the sample to the low-temperature chamber.

(a)   (b)
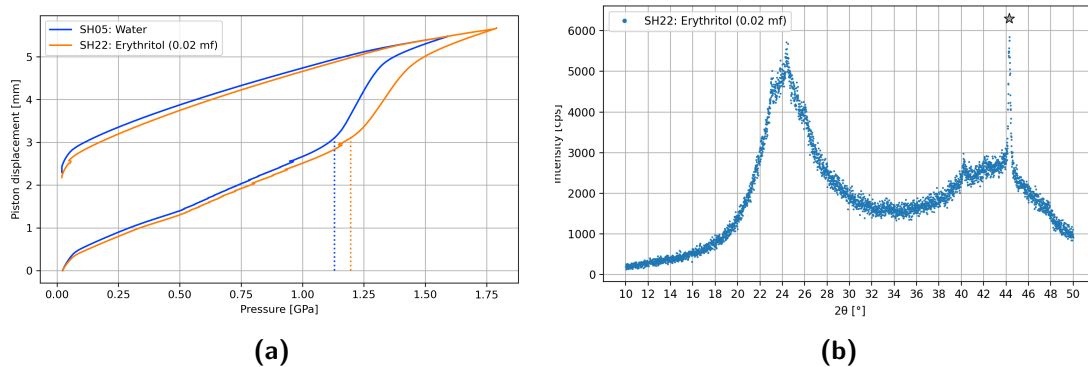
Figure 32: (a) Compression and subsequent decompression of the $0.02\,\mathrm{mf}$ erythritol solution at $78\,\mathrm{K}$ indicating the transition to uHDA and **(b)** the corresponding XRD measurement of the quenched sample

LDA $\leftrightarrow$ HDA transition

The VHDA samples of the $0.02\,\mathrm{mf}$ solution are prepared by annealing uHDA samples up to $\sim 140\,\mathrm{K}$ at a pressure of $1.09\,\mathrm{GPa}$. The resulting piston displacement curve and XRD measurement can be found in the appendix (Figure 40). Similar to the uHDA

sample, only an amorphous peak at $\sim 24°$ can be observed, which also may come from heat-induced transition to LDA during preparation for the XRD measurement.

The LDA sample made by decompression of VHDA at $140\,\text{K}$ undergoes a transition to a more dense state upon compression at $125\,\text{K}$ with an onset-pressure of $0.43\,\text{GPa}$ (Figure 33). This in accordance with the onset-pressure for the previously observed LDA $\rightarrow$ HDA transition.
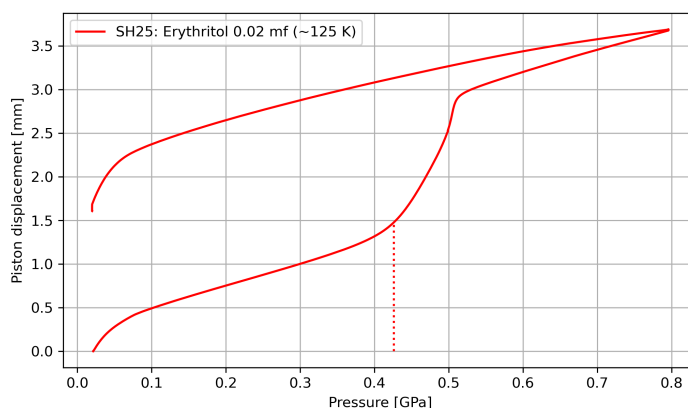
Figure 33: Compression of LDA sample from a $0.02\,\text{mf}$ erythritol solution at $125\,\text{K}$. The dotted line indicates the position of the onset-pressure for the transition to HDA.

Similar as for the $0.02\,\text{mf}$ sorbitol solution, this HDA state does not transform back to LDA upon decompression and has to be annealed from $125\,\text{K}$ to $140\,\text{K}$ at ambient pressure, resulting in a sharp decrease in density (Figure 34a).

The XRD measurement of the quench-recovered sample shows the expected amorphous maximum at $\sim 24°$, indicating the HDA sample transformed into LDA.

(a)   (b)
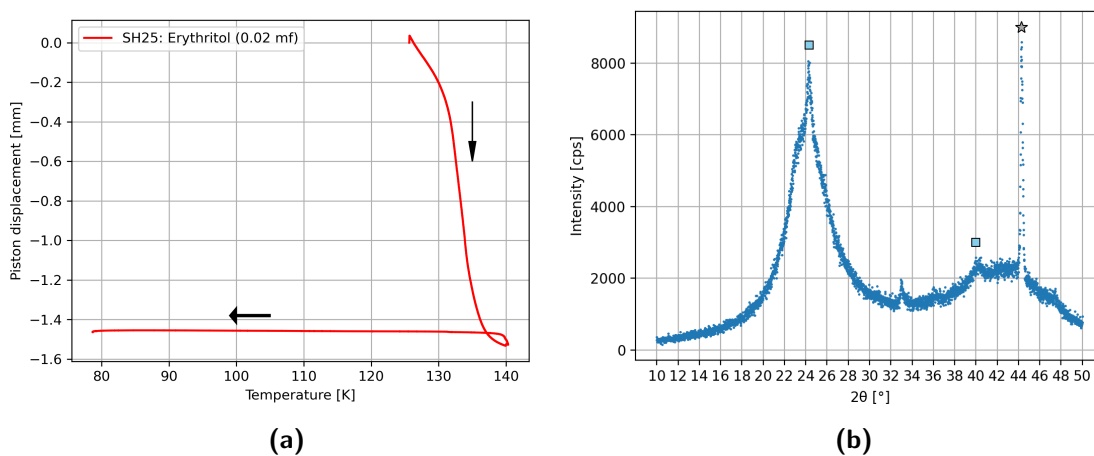
Figure 34: (a) Annealing the HDA sample from $125\,\text{K}$ to $140\,\text{K}$ indicating the transition to LDA, followed by quenching and **(a)** XRD measurement of the quench-recovered sample

5   Discussion

5.1   Results

Many results from previous experimental studies could be reproduced, like the observation that for increasing concentrations of the samples, the transition to uHDA for glycerol solutions occurs at higher onset-pressures (Figure 19). Also, the sharp transition within a small pressure range, becomes more continuous for increasing concentrations, possibly resulting in an incomplete transformation of the sample for more concentrated solutions upon compression to the maximum achievable pressure level. In the literature, this has been noted for glycerol solutions[30], but as Figure 28 and Figure 32a show, an analogous trend could be observed for the sorbitol and erythritol solutions.

Similar findings have been made for the LDA $\rightarrow$ HDA transition, where one expects a reversible first-order phase transition, as pointed out by Mishima[20]. So due to the relation $\left(\frac{\partial G}{\partial p}\right)_T = V$ from thermodynamics, sudden jumps in the volume and therefore in the piston displacement are anticipated during isothermal compression and decompression. This reversible transition between the two amorphs could be observed for the pure water (Figure 17) and the $0.02\,\mathrm{mf}$ glycerol solution (Figure 23) during compression and subsequent decompression for $T \lesssim 140\,\mathrm{K}$. For the $0.10\,\mathrm{mf}$ glycerol and the sorbitol solution, the hysteresis could also be observed at $T \approx 140\,\mathrm{K}$ but the transitions happen in a more continuous manner compared to the pure water samples. The same applies for the observed LDA $\rightarrow$ HDA transition for the $0.02\,\mathrm{mf}$ erythritol solution at $T \approx 125\,\mathrm{K}$.

The XRD measurements of the samples provided insights into their structures, leading to the interpretation that for glycerol solutions, the sudden shift of the onset-pressure for densification of the LDA samples from $\sim 0.40\,\mathrm{GPa}$ at $T \approx 140\,\mathrm{K}$ to $\sim 0.65\,\mathrm{GPa}$ at $T > 140\,\mathrm{K}$ indicates a pressure-induced crystallization into ice IX rather than the transition to HDA. Likewise, this crystallization was observed for the $0.02\,\mathrm{mf}$ sorbitol solutions at $T > 142\,\mathrm{K}$.

5.2   Conclusion and Outlook

In summary, the observations support the interpretation that aqueous solutions undergo phase separation into domains of maximally freeze-concentrated solution (MFCS) and hexagonal ice (I_h) upon cooling, as sketched in Figure 3.[30] The existence of such MFCS domains could explain the amorphous background with a maximum at $\sim 24°$ in the XRD measurement of the $0.10\,\mathrm{mf}$ glycerol solution upon cooling to $83\,\mathrm{K}$ (Figure 27b).

Also, the presence of this amorphous maximum at $24°$ in the XRD measurements of

samples which were compressed (Figure 20 and Figure 25b) could indicate that samples generated via PIA are still heterogenous with the ice I_h domains undergoing PIA to uHDA, while the MFCS domains are unaffected by the increase in pressure. Nevertheless, since LDA shows a first diffraction maximum in the same position, further studies are necessary to rule out one of the two options and fully understand the structure of dilute aqueous solutions upon cooling at ambient pressure.

The glycerol samples ultimately show no sign of the polyamorphic transition for temperatures $T \gtrsim 140 \, \mathrm{K}$ and similar for the $0.02 \, \mathrm{mf}$ sorbitol solution no transition to HDA could be observed for $T \gtrsim 142 \, \mathrm{K}$.

However, using pressure-vitrification (PVI) on emulsified solutions, Suzuki was able to observe the LDA $\leftrightarrow$ HDA transition up to $\sim 150 \, \mathrm{K}$ for glycerol and up to $\sim 153 \, \mathrm{K}$ for sorbitol solutions with a concentration of $0.02 \, \mathrm{mf}$.[27,28] It was also pointed out by Bachler et al. that PVI samples have a considerably higher crystallization temperature compared to samples made via PIA, for which the crystallization temperature is below the glass transition temperature of LDA and HDA.[26] Therefore, the homogenous samples made by PVI make a larger region of the phase diagram accessible compared to samples made via PIA. But implementing PVI in laboratory is more difficult, since one has to compress the liquid samples at $\sim 0.3 \, \mathrm{GPa}$ before cooling them.

Further studies using PIA on aqueous solutions could involve using different solutes or different concentrations, maybe solving the problem of phase separation upon cooling. This could also include studies on how the cooling rate affects the formation of the MFCS domains within the sample, even if the cooling rate is not high enough to vitrify the whole sample, since no attention was paid to this parameter in the context of this thesis.

List of Figures

List of Tables

Acronyms

I$_c$ cubic ice

I$_h$ hexagonal ice

ASW amorphous solid water

cps counts per second

eHDA expanded high-density amorphous ice

HDA high-density amorphous ice

HDL high-density liquid

HGW hyperquenched glassy water

LDA low-density amorphous ice

LDL low-density liquid

LLCP liquid-liquid critical point

LLT liquid-liquid transition

mf mole fraction

MFCS maximally freeze-concentrated solution

PIA pressure-induced amorphization

PVI pressure-vitrification

uHDA unannealed high-density amorphous ice

VHDA very-high-density amorphous ice

XRD X-ray diffraction

A   Specifications of the piston-cylinder apparatus

Component	Specifications
Steel cell	5 cm diameter 6 cm height 8 mm drill-hole in centre three 4 mm drill-holes for temperature control
Steel cylinder (small)	8 mm diameter 8 mm height
Steel cylinder (medium)	8 mm diameter 20 mm height
Steel cylinder (large)	8 mm diameter 38 mm height
Bakelite plate	35 mm width 35 mm length 10 mm height
Steel plate (small)	18 mm diameter 8 mm height
Steel plate (large)	28 mm diameter 8 mm height
Steel disc	127 mm diameter 20 mm height
Bakelite disc	248 mm diameter 10 mm height
Teflon disc	200 mm diameter 14 mm height
Pot	surrounded by thermally insulating foam
Indium container	made from a $0.2 \times 25 \times 25$ mm indium foil

Table 5: Specifications for the components of the piston-cylinder setup

B   Additional plots
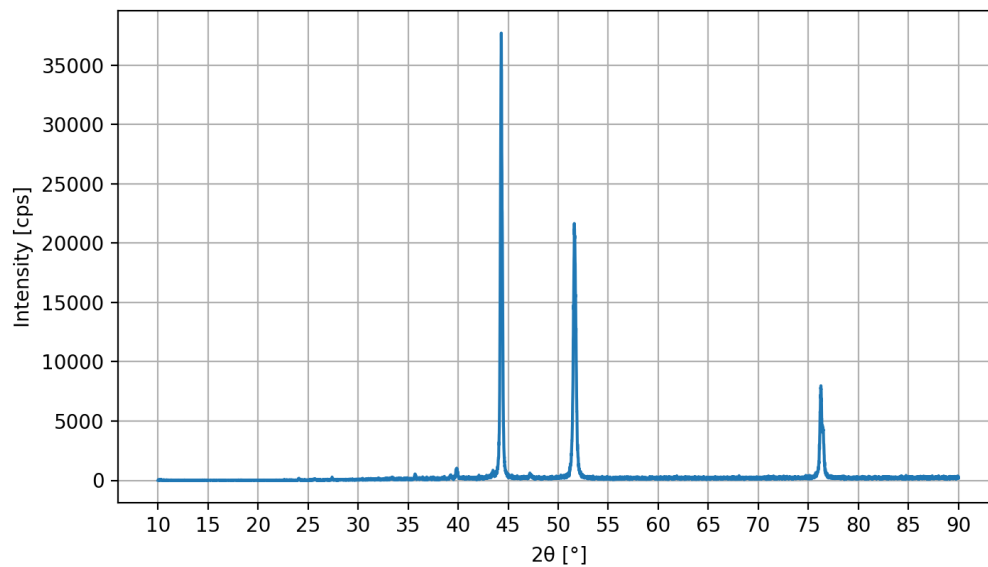
Figure 35: XRD measurement of the empty low-temperature chamber
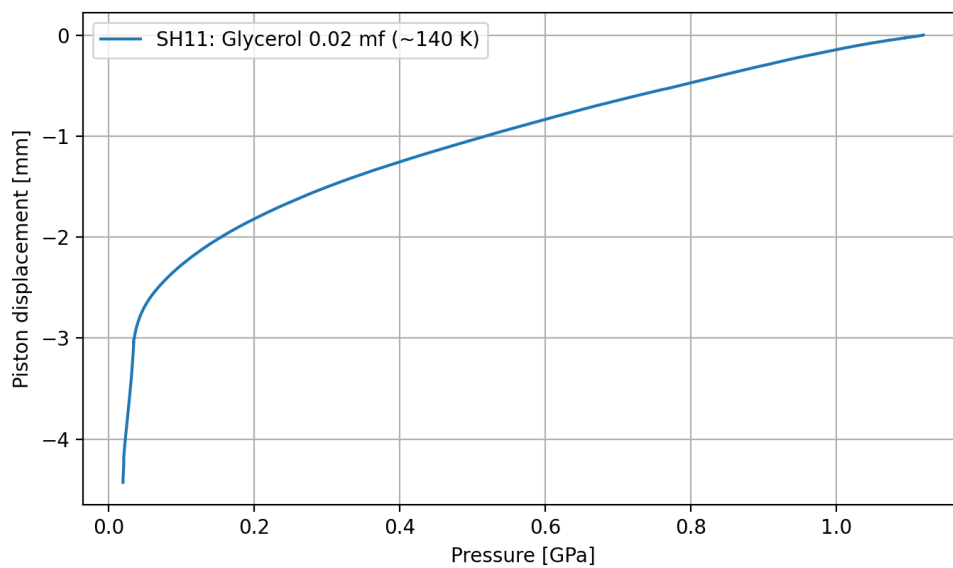
Figure 36: Decompression of VHDA from $1.09\,\mathrm{GPa}$ to $0.02\,\mathrm{GPa}$ at $140\,\mathrm{K}$, indicating the transition to LDA due to a rapid decrease in density
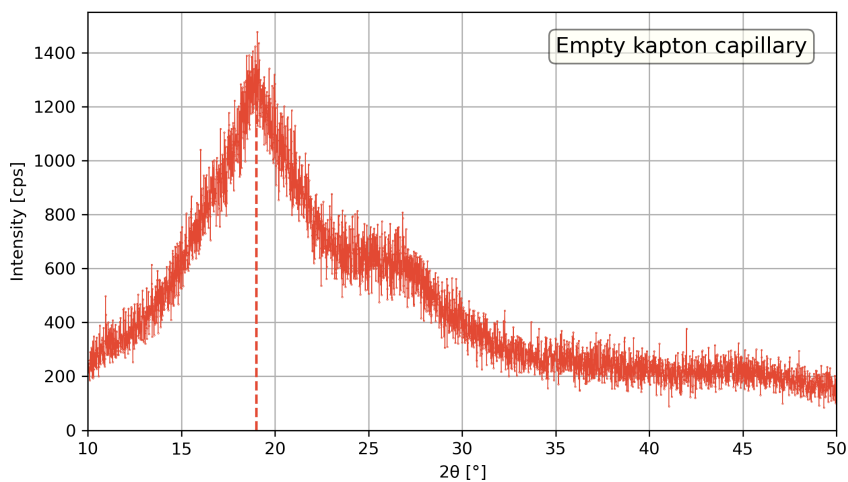
Figure 37: XRD measurement of an empty kapton capillary
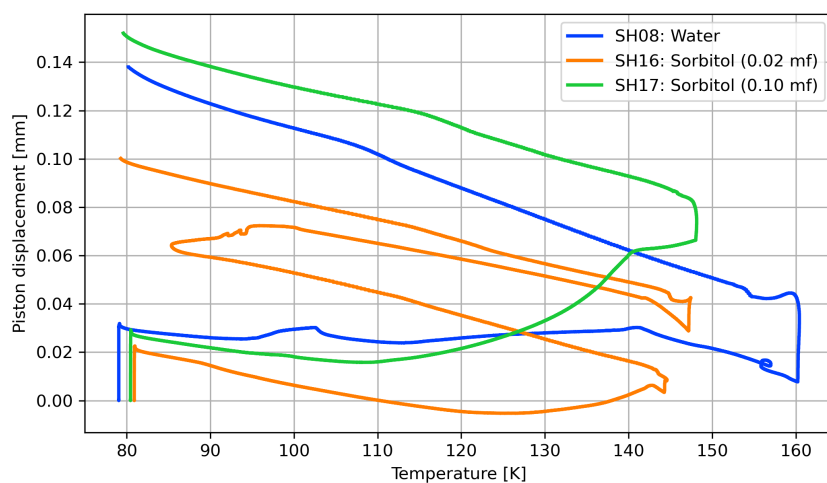
Figure 38: VHDA transition of sorbitol solutions for different mole fractions
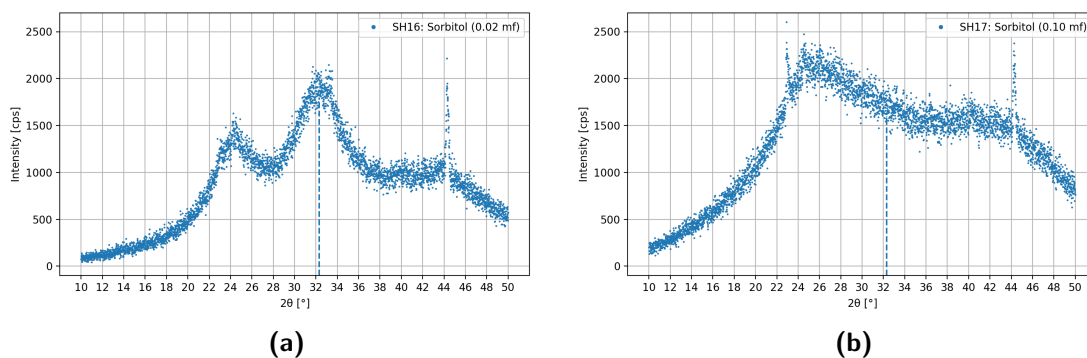
Figure 39: XRD measurement of the sample **(a)** SH16: Sorbitol $(0.02\,\text{mf})$ and **(b)** SH17: Sorbitol $(0.10\,\text{mf})$. A dashed line at $\sim 32°$ marks the position for the maximum of an expected VHDA sample which is only observed for the SH16 sample.
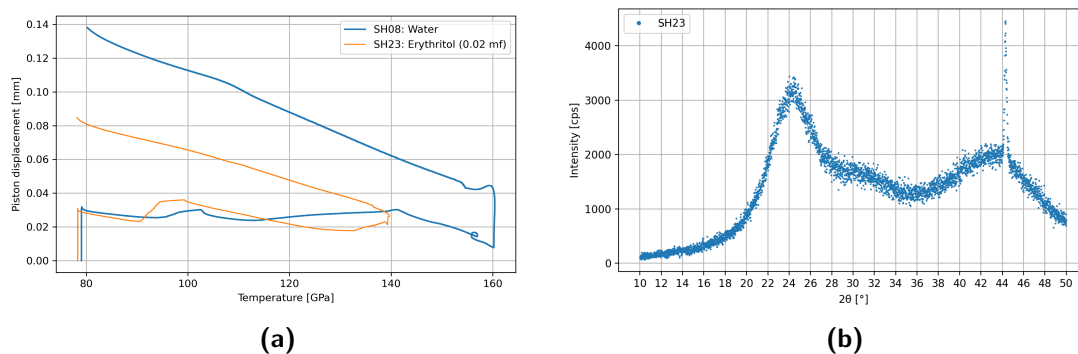
Figure 40: **(a)** Annealing the uHDA sample of $0.02\,\text{mf}$ erythritol solution up to $140\,\text{K}$ at $1.09\,\text{GPa}$ and **(b)** the corresponding XRD measurement of the quenched sample

C Determination of the onset-pressures

Sample	Fit 1	Fit 2	Onset-pressure [GPa]
SH05 Water	from 0.50 to 1.15 GPa $a_1 = (2.540 \pm 0.001)$ $b_1 = (0.126 \pm 0.001)$ reduced $\chi^2 = 1.12 \cdot 10^{-4}$	from 1.15 to 1.30 GPa $a_2 = (9.961 \pm 0.011)$ $b_2 = (-8.262 \pm 0.014)$ reduced $\chi^2 = 1.65 \cdot 10^{-4}$	(1.13 ± 0.02)
SH13 Glycerol (0.02 mf)	from 0.50 to 1.15 GPa $a_1 = (2.380 \pm 0.002)$ $b_1 = (0.118 \pm 0.002)$ reduced $\chi^2 = 1.45 \cdot 10^{-4}$	from 1.15 to 1.35 GPa $a_2 = (8.969 \pm 0.013)$ $b_2 = (-7.373 \pm 0.016)$ reduced $\chi^2 = 4.61 \cdot 10^{-4}$	(1.14 ± 0.02)
SH10 Glycerol (0.10 mf)	from 0.50 to 1.20 GPa $a_1 = (2.471 \pm 0.001)$ $b_1 = (0.081 \pm 0.001)$ reduced $\chi^2 = 1.38 \cdot 10^{-4}$	from 1.15 to 1.60 GPa $a_2 = (4.085 \pm 0.004)$ $b_2 = (-1.823 \pm 0.005)$ reduced $\chi^2 = 5.35 \cdot 10^{-4}$	(1.18 ± 0.01)
SH14 Glycerol (0.10 mf)	from 0.50 to 1.20 GPa $a_1 = (2.380 \pm 0.001)$ $b_1 = (0.274 \pm 0.001)$ reduced $\chi^2 = 1.19 \cdot 10^{-4}$	from 1.15 to 1.60 GPa $a_2 = (3.881 \pm 0.003)$ $b_2 = (-1.484 \pm 0.005)$ reduced $\chi^2 = 4.00 \cdot 10^{-4}$	(1.17 ± 0.01)
SH16 Sorbitol (0.02 mf)	from 0.50 to 1.15 GPa $a_1 = (2.553 \pm 0.001)$ $b_1 = (0.107 \pm 0.001)$ reduced $\chi^2 = 0.71 \cdot 10^{-4}$	from 1.20 to 1.40 GPa $a_2 = (7.182 \pm 0.007)$ $b_2 = (-5.348 \pm 0.009)$ reduced $\chi^2 = 1.27 \cdot 10^{-4}$	(1.18 ± 0.01)
SH21 Sorbitol (0.02 mf)	from 0.50 to 1.15 GPa $a_1 = (2.624 \pm 0.001)$ $b_1 = (0.391 \pm 0.001)$ reduced $\chi^2 = 1.63 \cdot 10^{-4}$	from 1.20 to 1.50 GPa $a_2 = (6.205 \pm 0.021)$ $b_2 = (-3.919 \pm 0.027)$ reduced $\chi^2 = 12.69 \cdot 10^{-4}$	(1.20 ± 0.04)
SH22 Erythritol (0.02 mf)	from 0.50 to 1.15 GPa $a_1 = (2.412 \pm 0.001)$ $b_1 = (0.103 \pm 0.001)$ reduced $\chi^2 = 0.67 \cdot 10^{-4}$	from 1.20 to 1.40 GPa $a_2 = (7.508 \pm 0.020)$ $b_2 = (-5.995 \pm 0.025)$ reduced $\chi^2 = 11.02 \cdot 10^{-4}$	(1.20 ± 0.03)

Table 6: Fit range, parameters, reduced χ^2 of the linear fits and determined onset-pressures for the uHDA transitions

Sample	Fit 1	Fit 2	Onset-pressure [GPa]
SH11 Glycerol (0.02 mf, ∼139 K)	from 0.20 to 0.38 GPa $a_1 = (3.061 \pm 0.009)$ $b_1 = (0.070 \pm 0.003)$ reduced $\chi^2 = 1.57 \cdot 10^{-4}$	from 0.40 to 0.42 GPa $a_2 = (43.41 \pm 0.70)$ $b_2 = (-15.77 \pm 0.28)$ reduced $\chi^2 = 6.02 \cdot 10^{-3}$	(0.39 ± 0.39)
SH11 Glycerol (0.02 mf, ∼143 K)	from 0.40 to 0.70 GPa $a_1 = (2.999 \pm 0.014)$ $b_1 = (-0.127 \pm 0.008)$ reduced $\chi^2 = 1.89 \cdot 10^{-3}$	from 0.70 to 0.85 GPa $a_2 = (8.720 \pm 0.023)$ $b_2 = (-3.893 \pm 0.018)$ reduced $\chi^2 = 6.26 \cdot 10^{-4}$	(0.66 ± 0.03)
SH12 Glycerol (0.10 mf, ∼ 140 K)	from 0.20 to 0.45 GPa $a_1 = (3.272 \pm 0.006)$ $b_1 = (-0.061 \pm 0.002)$ reduced $\chi^2 = 1.88 \cdot 10^{-4}$	from 0.45 to 0.55 GPa $a_2 = (6.122 \pm 0.026)$ $b_2 = (-1.275 \pm 0.013)$ reduced $\chi^2 = 2.48 \cdot 10^{-4}$	(0.43 ± 0.02)
SH12 Glycerol (0.10 mf, ∼ 145 K)	from 0.40 to 0.70 GPa $a_1 = (2.960 \pm 0.006)$ $b_1 = (-0.097 \pm 0.003)$ reduced $\chi^2 = 3.76 \cdot 10^{-4}$	from 0.70 to 0.85 GPa $a_2 = (4.920 \pm 0.003)$ $b_2 = (-1.421 \pm 0.002)$ reduced $\chi^2 = 9.17 \cdot 10^{-6}$	(0.68 ± 0.01)
SH15 Glycerol (0.10 mf, ∼ 134 K)	from 0.20 to 0.45 GPa $a_1 = (2.786 \pm 0.007)$ $b_1 = (0.129 \pm 0.002)$ reduced $\chi^2 = 3.02 \cdot 10^{-4}$	from 0.45 to 0.55 GPa $a_2 = (8.893 \pm 0.016)$ $b_2 = (-2.575 \pm 0.008)$ reduced $\chi^2 = 9.52 \cdot 10^{-5}$	(0.44 ± 0.01)
SH15 Glycerol (0.10 mf, ∼ 143 K)	from 0.40 to 0.70 GPa $a_1 = (2.855 \pm 0.005)$ $b_1 = (0.000 \pm 0.002)$ reduced $\chi^2 = 2.24 \cdot 10^{-4}$	from 0.70 to 0.85 GPa $a_2 = (5.715 \pm 0.014)$ $b_2 = (-1.957 \pm 0.011)$ reduced $\chi^2 = 2.22 \cdot 10^{-4}$	(0.68 ± 0.02)
SH19 Sorbitol (0.02 mf, ∼ 125 K)	from 0.20 to 0.40 GPa $a_1 = (2.943 \pm 0.008)$ $b_1 = (0.108 \pm 0.002)$ reduced $\chi^2 = 1.64 \cdot 10^{-4}$	from 0.43 to 0.48 GPa $a_2 = (15.32 \pm 0.09)$ $b_2 = (-5.115 \pm 0.042)$ reduced $\chi^2 = 3.73 \cdot 10^{-4}$	(0.42 ± 0.06)
SH20 Sorbitol (0.02 mf, ∼ 140 K)	from 0.20 to 0.38 GPa $a_1 = (4.275 \pm 0.035)$ $b_1 = (-0.210 \pm 0.010)$ reduced $\chi^2 = 1.97$	from 0.37 to 0.41 GPa $a_2 = (25.81 \pm 0.12)$ $b_2 = (-8.152 \pm 0.048)$ reduced $\chi^2 = 3.53 \cdot 10^{-4}$	(0.37 ± 0.07)
SH20 Sorbitol (0.02 mf, ∼ 142 K)	from 0.20 to 0.38 GPa $a_1 = (3.531 \pm 0.018)$ $b_1 = (-0.054\,84 \pm 0.005\,22)$ reduced $\chi^2 = 6.65 \cdot 10^{-4}$	from 0.37 to 0.40 GPa $a_2 = (17.52 \pm 0.13)$ $b_2 = (-5.222 \pm 0.050)$ reduced $\chi^2 = 1.70 \cdot 10^{-4}$	(0.37 ± 0.07)
SH26 Sorbitol (0.02 mf, ∼ 144 K)	from 0.20 to 0.65 GPa $a_1 = (2.947 \pm 0.005)$ $b_1 = (0.611 \pm 0.002)$ reduced $\chi^2 = 9.56 \cdot 10^{-4}$	from 0.65 to 0.75 GPa $a_2 = (8.886 \pm 0.034)$ $b_2 = (-3.245 \pm 0.024)$ reduced $\chi^2 = 4.16 \cdot 10^{-4}$	(0.65 ± 0.03)
SH25 Erythritol (0.02 mf, ∼ 125 K)	from 0.20 to 0.40 GPa $a_1 = (2.710 \pm 0.006)$ $b_1 = (0.197 \pm 0.002)$ reduced $\chi^2 = 9.49 \cdot 10^{-5}$	from 0.44 to 0.50 GPa $a_2 = (15.42 \pm 0.07)$ $b_2 = (-5.219 \pm 0.034)$ reduced $\chi^2 = 4.04 \cdot 10^{-4}$	(0.43 ± 0.05)

Table 7: Fit range, parameters, reduced χ^2 of the linear fits and determined onset-pressures for the LDA ↔ HDA transitions

D Fit parameters for Voigt functions

Sample	Fit range [°]	Fit parameters
SH05	20° to 28° (excluding Bragg reflexes)	amplitude: 18414.1600 +/- 441.054554 center: 24.1413151 +/- 0.01552628 sigma: 1.20086838 +/- 0.01876902 slope: 129.200833 +/- 3.78925711 intercept: -2250.83031 +/- 90.3727453 gamma: 1.20086838 +/- 0.01876902 fwhm: 4.32467605 +/- 0.06759270 height: 3200.35581 +/- 31.8185568 reduced chi-square = 18104.8576
SH04	29° to 36°	amplitude: 790.850437 +/- 90.1499302 center: 32.4630289 +/- 0.06027071 sigma: 0.99383335 +/- 0.07328525 slope: 10.8902584 +/- 1.31689704 intercept: -165.766149 +/- 44.1568577 gamma: 0.99383335 +/- 0.07328525 fwhm: 3.57908273 +/- 0.26392149 height: 166.081996 +/- 8.27673776 reduced chi-square = 2116.99719
SH07	20° to 28° (excluding Bragg reflexes)	amplitude: 4470.10994 +/- 77.4964284 center: 23.8971701 +/- 0.01192009 sigma: 0.81728392 +/- 0.01304081 slope: 24.2414753 +/- 1.33746624 intercept: -310.904901 +/- 34.2137487 gamma: 0.81728392 +/- 0.01304081 fwhm: 2.94327693 +/- 0.04696374 height: 1141.52916 +/- 10.2145095 reduced chi-square = 4814.01602
Pure glycerol (298 K)	18.5° to 22.0°	amplitude: 9103.97602 +/- 4404.69796 center: 20.2444252 +/- 0.08723642 sigma: 1.11947942 +/- 0.21868811 slope: 99.9999986 +/- 26.0294505 intercept: -1013.31283 +/- 928.232466 gamma: 1.11947942 +/- 0.21868811 fwhm: 4.03157076 +/- 0.78755946 height: 1697.29273 +/- 490.853123 reduced chi-square = 17343.0368

Sample	Fit range [°]	Fit parameters
Pure glycerol (250 K)	18.5° to 22.0°	amplitude: 7834.63119 +/- 2605.96849 center: 20.4164968 +/- 0.06987420 sigma: 1.01450180 +/- 0.13963732 slope: 99.9999961 +/- 32.6574190 intercept: -1100.93495 +/- 574.032259 gamma: 1.01450180 +/- 0.13963732 fwhm: 3.65351583 +/- 0.50287456 height: 1611.78644 +/- 315.700395 reduced chi-square = 13897.8577
Pure glycerol (200 K)	18.5° to 22.0°	amplitude: 7289.23443 +/- 2390.51427 center: 20.6367595 +/- 0.09036969 sigma: 0.98608675 +/- 0.12801290 slope: 99.9999998 +/- 14.7649826 intercept: -1218.28949 +/- 742.496864 gamma: 0.98608675 +/- 0.12801290 fwhm: 3.55118499 +/- 0.46101167 height: 1542.79618 +/- 307.565213 reduced chi-square = 11289.6611
Pure glycerol (148 K)	19.0° to 22.5°	amplitude: 5965.64593 +/- 1926.36730 center: 20.7752406 +/- 0.02935656 sigma: 0.97350910 +/- 0.13412536 slope: 99.9999999 +/- 19.6704542 intercept: -1239.33713 +/- 331.561383 gamma: 0.97350910 +/- 0.13412536 fwhm: 3.50588920 +/- 0.48302441 height: 1278.96665 +/- 238.010894 reduced chi-square = 11755.4891
Pure glycerol (100 K)	19.0° to 22.5°	amplitude: 4073.52622 +/- 1184.47061 center: 20.7741102 +/- 0.05856374 sigma: 0.86504839 +/- 0.11345911 slope: 100.0000000 +/- 0.01850263 intercept: -1105.50951 +/- 431.727243 gamma: 0.86504839 +/- 0.11345911 fwhm: 3.11529066 +/- 0.40859923 height: 982.815225 +/- 158.398842 reduced chi-square = 12332.7292

Sample	Fit range [°]	Fit parameters
Pure glycerol (83 K)	19.0° to 22.5°	amplitude: 4756.57923 +/- 1559.32689
		center: 20.7528435 +/- 0.06047946
		sigma: 0.94602023 +/- 0.13401945
		slope: 99.9999999 +/- 21.6545610
		intercept: -1244.79234 +/- 455.932992
		gamma: 0.94602023 +/- 0.13401945
		fwhm: 3.40689378 +/- 0.48264299
		height: 1049.38795 +/- 196.524704
		reduced chi-square = 9853.95952

Table 8: Fit range, parameters, reduced χ^2 of the Voigt fits used to determine the position of the maximum in the XRD measurements

E Specifications of the used capillaries

Material	Manufacturer	Outside diameter [mm]	Wall thickness [mm]
Glass Nr. 50	hilgenberg	1.5	0.1
Polymide (Kapton)	Cole-Parmer	0,960	0,046

Table 9: Capillaries used for the X-ray study of glycerol, water and glycerol solution ($0.10\,\mathrm{mf}$)

References

[1] SWR2 Archivradio, *Kernphysik: berühmte Physiker plaudern über deren Anfänge*, https://www.swr.de/swr2/wissen/archivradio/kernphysik-beruehmte-physiker-plaudern-ueber-anfaenge-100.html, 2019.

[2] M. Chaplin, *Anomalous properties of water*, 2020.

[3] O. Mishima, "Polyamorphism in water", Proceedings of the Japan Academy. Series B, Physical and Biological Sciences **86**, 165–175 (2010).

[4] P. Gallo, K. Amann-Winkel, C. A. Angell, M. A. Anisimov, F. Caupin, C. Chakravarty, E. Lascaris, T. Loerting, A. Z. Panagiotopoulos, J. Russo, J. A. Sellberg, H. E. Stanley, H. Tanaka, C. Vega, L. Xu, and L. G. M. Pettersson, "Water: A Tale of Two Liquids", Chemical Reviews **116**, 7463–7500 (2016).

[5] T. C. Hansen, "The everlasting hunt for new ice phases", Nature Communications **12**, 3161 (2021).

[6] O. Mishima, L. D. Calvert, and E. Whalley, "'Melting ice' I at 77 K and 10 kbar: a new method of making amorphous solids", Nature **310**, 393–395 (1984).

[7] E. F. Burton and W. F. Oliver, "The Crystal Structure of Ice at Low Temperatures", Proceedings of the Royal Society of London. Series A, Mathematical and Physical Sciences **153**, 166–172 (1935).

[8] P. Brüggeller and E. Mayer, "Complete vitrification in pure liquid water and dilute aqueous solutions", Nature **288**, 569–571 (1980).

[9] D. Cressey and E. Callaway, "Cryo-electron microscopy wins chemistry Nobel", Nature **550**, 167 (2017).

[10] I. Kohl, L. Bachmann, A. Hallbrucker, E. Mayer, and T. Loerting, "Liquid-like relaxation in hyperquenched water at ¡ or = 140 K", Physical chemistry chemical physics : PCCP **7**, 3210–3220 (2005).

[11] E. F. Burton and W. F. Oliver, "X-Ray Diffraction Patterns of Ice", Nature **135**, 505–506 (1935).

[12] D. T. Bowron, J. L. Finney, A. Hallbrucker, I. Kohl, T. Loerting, E. Mayer, and A. K. Soper, "The local and intermediate range structures of the five amorphous ices at 80 K and ambient pressure: a Faber-Ziman and Bhatia-Thornton analysis", The Journal of Chemical Physics **125**, 194502 (2006).

[13] E. Mayer, "New method for vitrifying water and other liquids by rapid cooling of their aerosols", Journal of Applied Physics **58**, 663–667 (1985).

[14] O. Mishima, L. D. Calvert, and E. Whalley, "An apparently first-order transition between two amorphous phases of ice induced by pressure", Nature **314**, 76–78 (1985).

[15] K. Winkel, D. T. Bowron, T. Loerting, E. Mayer, and J. L. Finney, "Relaxation effects in low density amorphous ice: two distinct structural states observed by neutron diffraction", The Journal of Chemical Physics **130**, 204502 (2009).

[16] K. Winkel, M. S. Elsaesser, E. Mayer, and T. Loerting, "Water polyamorphism: reversibility and (dis)continuity", The Journal of Chemical Physics **128**, 044510 (2008).

[17] K. Winkel, M. Bauer, E. Mayer, M. Seidl, M. S. Elsaesser, and T. Loerting, "Structural transitions in amorphous H_2O and D_2O: the effect of temperature", Journal of Physics: Condensed Matter **20**, 494212 (2008).

[18] T. Loerting, C. Salzmann, I. Kohl, E. Mayer, and A. Hallbrucker, "A second distinct structural "state" of high-density amorphous ice at 77 K and 1 bar", Physical Chemistry Chemical Physics **3**, 5355–5357 (2001).

[19] R. J. Nelmes, J. S. Loveday, T. Strässle, C. L. Bull, M. Guthrie, G. Hamel, and S. Klotz, "Annealed high-density amorphous ice under pressure", Nature Physics **2**, 414–418 (2006).

[20] O. Mishima, "Reversible first–order transition between two H_2O amorphs at $\sim$0.2 GPa and $\sim$135 K", The Journal of Chemical Physics **100**, 5910–5912 (1994).

[21] T. Loerting, K. Winkel, M. Seidl, M. Bauer, C. Mitterdorfer, P. H. Handle, C. G. Salzmann, E. Mayer, J. L. Finney, and D. T. Bowron, "How many amorphous ices are there?", Physical Chemistry Chemical Physics **13**, 8783–8794 (2011).

[22] T. Loerting, W. Schustereder, K. Winkel, C. G. Salzmann, I. Kohl, and E. Mayer, "Amorphous ice: stepwise formation of very-high-density amorphous ice from low-density amorphous ice at 125 K", Physical Review Letters **96**, 025702 (2006).

[23] O. Mishima, "Relationship between melting and amorphization of ice", Nature **384**, 546–549 (1996).

[24] K. Amann-Winkel, R. Böhmer, F. Fujara, C. Gainaru, B. Geil, and T. Loerting, "Colloquium: Water's controversial glass transitions", Rev. Mod. Phys. **88**, 011002 (2016).

[25] P. H. Poole, F. Sciortino, U. Essmann, and H. E. Stanley, "Phase behaviour of metastable water", Nature **360**, 324–328 (1992).

[26] J. Bachler, P. H. Handle, N. Giovambattista, and T. Loerting, "Glass polymorphism and liquid-liquid phase transition in aqueous solutions: experiments and computer simulations", Physical Chemistry Chemical Physics **21**, 23238–23268 (2019).

[27] Y. Suzuki and O. Mishima, "Experimentally proven liquid-liquid critical point of dilute glycerol-water solution at 150 K", The Journal of Chemical Physics **141**, 094505 (2014).

[28] Y. Suzuki, "Effect of solute nature on the polyamorphic transition in glassy polyol aqueous solutions", The Journal of chemical physics **147**, 064511 (2017).

[29] Y. Suzuki, "Experimental estimation of the location of liquid-liquid critical point for polyol aqueous solutions", The Journal of chemical physics **149**, 204501 (2018).

[30] J. Bachler, V. Fuentes-Landete, D. A. Jahn, J. Wong, N. Giovambattista, and T. Loerting, "Glass polymorphism in glycerol-water mixtures: II. Experimental studies", Physical Chemistry Chemical Physics **18**, 11058–11068 (2016).

[31] H. Ibach and H. Lüth, *Festkörperphysik: Einführung in die Grundlagen ; mit 18 Tafeln und 104 Übungen*, 7. Aufl., Springer-Lehrbuch (Springer, Berlin and Heidelberg, 2009), page 62.

[32] Wikipedia, *Powder diffraction*, https://en.wikipedia.org/w/index.php?title=Powder_diffraction&oldid=1159111989, 2023.

[33] Wikipedia, *Water*, https://en.wikipedia.org/w/index.php?title=Water&oldid=1170621419, 2023.

[34] Wikipedia, *Water (data page)*, https://en.wikipedia.org/w/index.php?title=Water_(data_page)&oldid=1153960609, 2023.

[35] Wikipedia, *Sorbitol*, https://en.wikipedia.org/w/index.php?title=Sorbitol&oldid=1162421685, 2023.

[36] Wikipedia, *Erythrit*, https://de.wikipedia.org/w/index.php?title=Erythrit&oldid=236428568, 2023.

[37] M. Kumai, "Hexagonal and cubic ice at low temperatures", Journal of Glaciology **7**, 95–108 (1968).

[38] v. d. Jović, V. Maksimović, M. G. Pavlović, and K. I. Popov, "Morphology, internal structure and growth mechanism of electrodeposited Ni and Co powders", Journal of Solid State Electrochemistry **10**, 373–379 (2006).

[39] A. Fayter, S. Huband, and M. I. Gibson, "X-ray diffraction to probe the kinetics of ice recrystallization inhibition", Analyst **145**, 3666–3677 (2020).

[40] C. M. Tonauer, M. Bauer, and T. Loerting, "The impact of temperature and unwanted impurities on slow compression of ice", Physical Chemistry Chemical Physics **24**, 35–41 (2021).

[41] R. Zondervan, F. Kulzer, G. C. G. Berkhout, and M. Orrit, "Local viscosity of supercooled glycerol near T_g probed by rotational diffusion of ensembles and single dye molecules", Proceedings of the National Academy of Sciences of the United States of America **104**, 12628–12633 (2007).